Master of Science dissertation:

Image-Based Partial-Volume Correction in SPECT

Application to ^{177}Lu radionuclide therapy

Gustav Brolin

Supervisors:

Michael Ljungberg
Katarina Sjögreen Gleisner

Department of Medical Radiation Physics, Clinical Sciences, Lund
Lund University, Sweden, 2011

Abstract

Introduction and aim: In SPECT imaging, the finite spatial resolution of the imaging system leads to a blurring of the reconstructed image. Consequently, counts originating from each point in the source distribution will be spread out over a volume in the reconstructed image, leading to spill-over of counts between different structures and distortion of the apparent activity concentration. This process, which can seriously impair the accuracy in quantitative analysis, is termed the partial-volume effect. The magnitude of this effect depends on many factors but is generally determined by the size of the object of interest in relation to the spatial resolution of the system. At Skåne University Hospital, radionuclide therapy with ^{177}Lu-Tyr3-Octreotate is currently used for treatment of metastatic neuroendocrine tumors. Quantitative SPECT is utilized for treatment planning and dose assessment, focused on the kidneys which are the primary organs at risk. However, the activity concentration in the kidneys is believed to be underestimated because of the partial-volume effect. The aim of this work was to develop an accurate, robust and practical method to correct for the partial-volume effect in ^{177}Lu SPECT imaging.

Material and Methods: An image-based method for partial-volume correction (PVC) was developed for the current application, based on the *template projection – reconstruction method*. In this method, a number of structures with expected homogenous activity uptake are outlined on an anatomical or functional tomographic image. All voxels within a particular structure is assigned a value of unity, to form a *template*. This template is then projected into a set of planar images with an analytical projector, at angles corresponding to those used in SPECT acquisition. The projector models the effects of attenuation and distance-dependent resolution, which are thus included in the projection images. After reconstruction of the projection images, voxel-specific correction factors are obtained and used in an iterative algorithm to perform PVC on the SPECT image. The templates were reconstructed using a perturbation based method. The developed PVC method was evaluated in a Monte Carlo simulation study with SIMIND, using the XCAT phantom to generate source distributions resembling a patient being treated with ^{177}Lu-Tyr3-Octreotate at four different times post-injection. Additional testing of the PVC algorithm and reconstruction methods for the templates was performed with a digital geometrical phantom. Finally, the PVC method was applied on four clinical images to assure its practical functionality and compare the results with the results from the phantom study.

Results: In absence of noise and scattered photons, a nearly perfect correction was achieved for the geometrical phantom when the perturbation based reconstruction was used for the templates. In this case the source distribution and templates were perfectly spatially aligned and projected using the same projector. In the XCAT phantom study, the PVC reduced the error in kidney activity concentration from approximately -20 % to -1 % with templates acquired from the true organ configuration in the phantom. To study a more realistic scenario, the kidney VOI and template was also determined by automatic segmentation of the simulated SPECT image. In this case, the error was also considerably improved, from approximately -22 % to 2 % with PVC. For the clinical images, the count levels in the kidneys were in all four images approximately 5-10 % higher after PVC than the count levels obtained with the standard clinical method. The results were however sensitive to the outlining of the kidney VOI used to create the template. Similar results were obtained with both manual and automatic segmentation, as long as the shape and volume of the VOI corresponded to the anatomical shape of the kidney with reasonable accuracy.

Conclusions: A robust and practical method to correct for the partial-volume effect in ^{177}Lu SPECT imaging has been developed and evaluated. The method requires outlining of a number of structures with expected homogenous activity uptake. It was shown to perform well in a simulation study, and considerably reduced the bias in estimated activity concentration. Further evaluation is needed to investigate the sensitivity of non-homogenous activity uptake within the defined structures and if the number of outlined structures can be reduced with preserved quantitative accuracy. Physical phantom measurements should also be performed to validate the method. The method can easily be extended and used for other applications of quantitative SPECT.

Contents

List of abbreviations

1D	One-dimensional
2D	Two-dimensional
3D	Three-dimensional
CDRF	Collimator Detector Response Function
COR	Center of Rotation
CT	Computed Tomography
DR	Direct Reconstruction
ESSE	Effective Source Scatter Estimation
ET	Emission Tomography
FBP	Filtered Backprojection
FOV	Field-of-View
FWHM	Full Width at Half Maximum
GRF	Geometric Response Function
IRF	Intrinsic Response Function
MEGP	Medium Energy General Purpose
ML-EM	Maximum-Likelihood Expectation-Maximization
OS-EM	Ordered-Subset Expectation-Maximization
PBR	Perturbation Based Reconstruction
PET	Positron Emission Tomography
PMT	Photomultiplier Tube
PRRT	Peptide Receptor Radionuclide Therapy
PSF	Point Spread Function
PV	Partial-Volume
PVC	Partial-Volume Correction
PVE	Partial-Volume Effect
SNR	Signal-to-Noise Ratio
SPECT	Single Photon Emission Computed Tomography
VOI	Volume of Interest

1. Introduction

Radionuclide therapy is a treatment option for a number of malignant and benign diseases. As the name suggests, the therapy involves administration of a radioactive isotope to the patient, for instance by oral intake or intravenous injection. In Sweden 2010, approximately 3000 treatments were given for various conditions, such as ^{131}I against hyperthyroidism and thyroid cancer, ^{32}P against polycythemia and ^{89}Sr for pain relief for patients with skeletal metastases [1]. In order to optimize the treatment, *i.e.* maximize efficacy and minimize adverse side effects, individual dose planning and dose assessment is required. This is made possible by quantitative nuclear medicine imaging, for instance performed with a scintillation camera, which allows absolute quantification of the radionuclide uptake in different organs and tissues and thereby enabling patient specific dosimetry calculations. There are however several imaging degrading factors which seriously impacts the possibility for quantitative analysis. These include attenuation and scattering of photons in the patient and the limited spatial resolution of the imaging system. The limited spatial resolution causes activity from a certain point in the source distribution (patient), to be spread over a volume in the reconstructed tomographic image. This means that activity from adjacent organs and regions will "spill over" to each other, and also that the activity concentrations in objects small compared to the spatial resolution of the imaging system will be underestimated. This is called the partial-volume effect (PVE). The magnitude of this effect will depend on the shape and size of the organs, the differences in activity concentrations between the organs, and the spatial resolution of the imaging system. To improve quantitative accuracy, partial-volume correction (PVC) may be required.

A relatively new treatment option for selected patients with metastatic neuroendocrine tumors is peptide receptor radionuclide therapy (PRRT) [2-4]. These tumors often express somatostatin receptors, making it possible to target them using a radiolabeled somatostatin analogue. There are several possible radionuclide peptide combinations that can be used for imaging and/or therapy. At Skåne University Hospital in Lund, planar scintigraphic imaging is performed with ^{111}In-DTPA Octreotide to determine if the somatostatin receptor density is sufficiently high for the patient to be a suitable candidate for PRRT. The conjugate used for treatment is ^{177}Lu-Tyr3-Octreotate. ^{177}Lu is a beta-particle emitter, making it suitable for therapy, but in the decay there is also a 208 keV gamma photon emitted (n_γ =10.4 %), allowing quantitative SPECT imaging during the treatment course. The dose-limiting organ for this treatment is the kidneys, due to retention of the peptide in the renal cortex [2-4]. The absorbed dose in the kidneys should not exceed 27 Gy, according to current consensus protocol. Several different therapy administrations protocols exist, but are often based on injection of standard activities. At Skåne University Hospital in Lund, the amount of administered activity is 7.4 GBq per treatment cycle. The patients are given 3 or 4 treatments, depending on if the calculated cumulated absorbed dose to the kidneys exceeds 27 Gy or not. When using single photon emission computed tomography (SPECT) for dosimetry calculations, there is reason to believe that the partial-volume effect could lead to an underestimation of activity concentration and thus the absorbed dose to the kidneys.

Correction methods relying on physical phantom experiments are commonly used to correct for PVE [5]. These often involves the use of recovery coefficients, defined as the ratio between measured and true activity, and are typically measured in standard geometries with simple geometrical shapes (e. g. spheres, cylinders). Recovery coefficients are dependent on a number of factors such as object size and shape, object-to-background activity ratio and reconstruction parameters. The major drawback with this approach is that not all anatomical structures can be well approximated by simple geometrical shapes. In addition to this, a large number of measurements have to be made to account for all different combinations of radionuclide, collimator type, object size, object-to-background activity ratio etc.

The aim of this work was to investigate the impact of the partial-volume effect in ^{177}Lu SPECT imaging with focus on renal activity quantification, and to develop and evaluate an accurate, robust and practical correction method. The methodology selected and further developed is the template projection-reconstruction method, previously described in the context of cardiac perfusion [6, 7], oncology [8-10] and cerebral perfusion [11] SPECT. By modeling the image formation process, *i.e.* the acquisition of projection images and reconstruction of SPECT slices, the spill-over contribution of activity between different structures of interest can be estimated and corrected for. This methodology has also the advantage of inherently taking into account the size and shape of the anatomical structure, as well as the object-to-background activity ratio. In this work, the accuracy of the PVC method as a part of quantitative ^{177}Lu SPECT was evaluated in a Monte Carlo simulation study using the digital extended cardiac-torso phantom (XCAT) [12, 13] to generate source distributions realistic for patients being treated with ^{177}Lu-Octreotate. Different from several of the previous studies, this work has been mainly focused on developing a practical method and evaluating it under realistic clinical conditions. The influence of the segmentation method used for VOI definition has been investigated. The correction method requires accurate estimates of mean count levels in the pre-defined structures of interest (*e.g.* organs), which can be difficult to obtain since the volumes in the uncorrected SPECT image are affected by the partial-volume effect, and the apparent activity concentration is hence distorted. To overcome this problem, an iterative method for refinement of mean count levels was also developed and evaluated.

1.1 Principles of scintillation camera imaging

The scintillation camera is an instrument for visualizing the distribution of photon-emitting sources of radioactivity. The principal design was proposed by Hal O Anger in 1958, which is why it is often referred to as an "Anger Camera" [14]. The principal components of a scintillation camera are illustrated in Figure 1. It consists of a large scintillation crystal with a high cross-section for photoelectric interactions, which effectively absorbs photons and converts the absorbed photon energy into visible light. The most common crystal material is sodium iodide doped with a small amount of thallium; NaI(Tl). The visible light produced in the crystal is subsequently collected and transformed to an electrical signal which is amplified through an array of photomultiplier tubes (PMTs). Because of the use of multiple PMTs it is also possible to determine at which point in the crystal the interaction took place. The output of the PMTs is processed using "Anger logic" electronics, determining the spatial position and energy for each photon interacting in the crystal by calculating the centroid of the signals from each PMT knowing its relative position on the crystal. Usually, an energy acceptance window is employed to discard all photons that have been scattered in the object or collimator. However, due to the limited energy resolution of scintillation detectors, a large fraction of primary photons will also be rejected if the size of the energy window is chosen to small, resulting in clinically unacceptable examination times. The size of the window must therefore be chosen as a compromise.

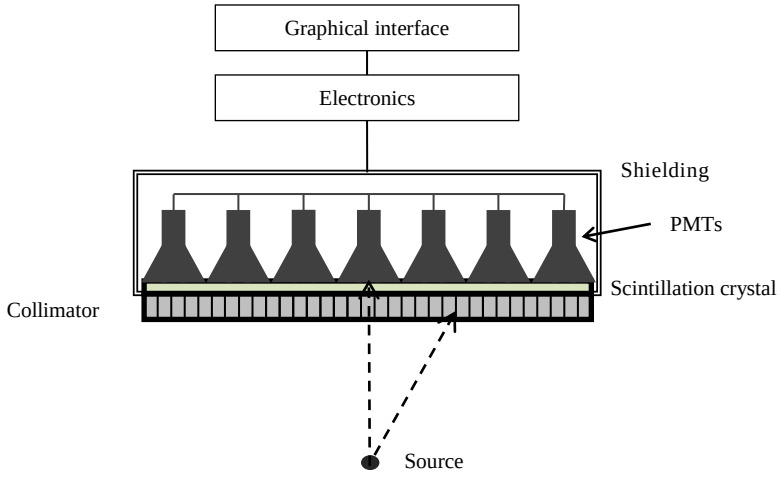

Figure 1: Schematic illustration of a scintillation camera with parallel-hole collimator. See text for further explanation.

The camera system is also equipped with some type of collimator which forms the image by selective absorption and transmission of photons. A collimator is usually made of lead or tungsten, and only transmits photon that travels in certain directions. For instance, the collimator depicted in Figure 1 has parallel holes and only transmits photons incident approximately normal to the collimator face. If the incidence angle is larger than a certain acceptance angle, the photon will be absorbed in the collimator walls (septa). The collimator design is crucial for the performance of the imaging system, and must be optimized for different photon energies to prevent photons from penetrating the collimator walls. The spatial resolution of a scintillation camera is largely determined by the properties of the collimator. There is also a compromise between sensitivity and resolution. A high resolution collimator absorbs a larger fraction of incident photons than a low resolution collimator and has thus a lower sensitivity, which can lead to longer acquisition times or increased image noise.

1.1.1 Drawbacks with planar imaging

In conventional scintillation camera imaging, a three-dimensional (3D) activity distribution within the patient is depicted as a two-dimensional (2D) projection image. This is often referred to as planar imaging, and gives no information about the activity distribution in the depth dimension, resulting in difficulties resolving the contribution to the total signal from different overlapping structures. This has consequences in terms of limited image contrast and reduced accuracy in quantitative analysis. For instance, the liver and right kidney can be overlapping in the posterior-anterior direction, making it difficult to separate counts originating from either one of these organs in a frontal planar projection image. Furthermore, activity quantification is often performed by means of the conjugate view method, which requires knowledge of the source extension in the depth dimension [15, 16]. These shortcomings of planar imaging can be overcome with SPECT (Single Photon Computed Tomography), which gives images of the activity distribution in three dimensions. Planar imaging have however some advantages compared to SPECT, as it is less complex, faster and allows imaging over a larger field-of-view (FOV).

1.1.2 Single Photon Emission Computed Tomography

As previously mentioned, a 3D representation of the activity distribution within a patient can be obtained by means of SPECT. This is accomplished by rotating the camera around the patient and acquiring a large set of planar projection images at different angles. The projection data is used in a mathematical reconstruction algorithm, to calculate the source distribution in 3D. The resulting 2D images are tomographic, meaning that they represent thin slices of the 3D source volume.

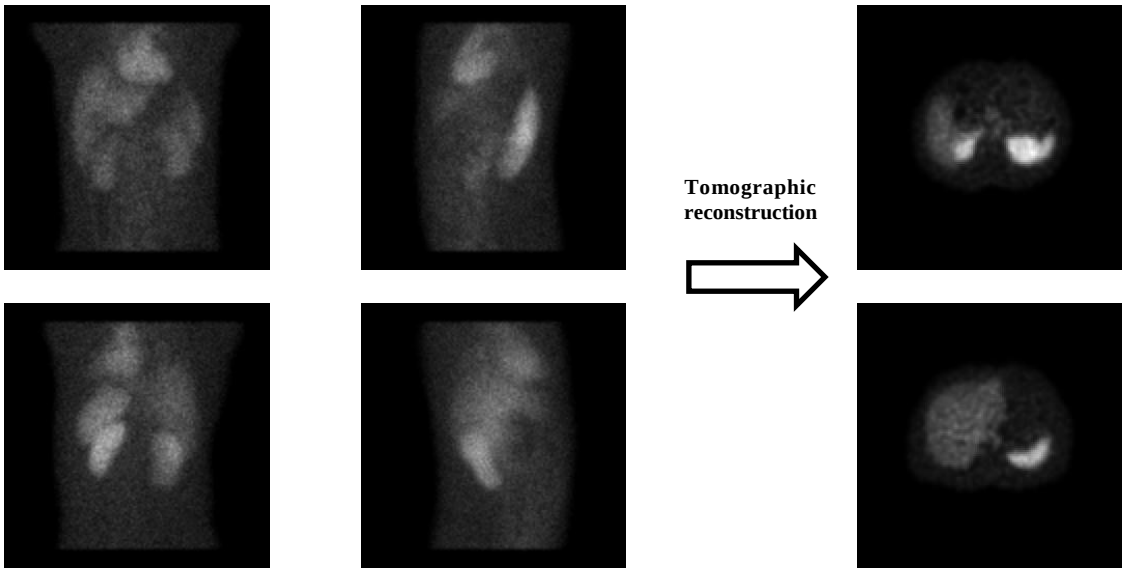

Figure 2: Schematic illustration of SPECT imaging. A large set of projection images (left) are acquired and used in reconstruction algorithm to calculate the source distribution in 3D, shown here as transversal slices (right).

The 3D true source distribution can be considered to be composed of a number of 2D slices, $f(x,y)$. Since the camera is rotating around the patient, it is convenient to define a rotated coordinate system (s,t), with the axis parallel and perpendicular to the camera face, respectively. The relation between the two coordinate systems is for counterclockwise rotation hence given by:

$$\begin{bmatrix} s \\ t \end{bmatrix} = \begin{bmatrix} \cos\theta & \sin\theta \\ -\sin\theta & \cos\theta \end{bmatrix} \begin{bmatrix} x \\ y \end{bmatrix} \quad \text{Eq. 1}$$

as depicted in Figure 3 below. The acquisition of projection images can in the absence of image degrading effects, such as attenuation, scatter and imperfect detector response, be described mathematically as

$$p_\theta(s) = \int_{-\infty}^{\infty} f(s,t)dt \quad \text{Eq. 2}$$

where p_θ is the acquired one-dimensional (1D) projection at angle θ. This is sometimes referred to as ideal imaging [17]. In terms of the original coordinate system, Eq. 2 can be written as

$$p_\theta(s) = \int_{-\infty}^{\infty}\int_{-\infty}^{\infty} f(x,y)\delta(x\cos\theta + y\sin\theta - s)\,dxdy \quad \text{Eq. 3}$$

Eq. 2 and 3 is the 2D Radon transform of $f(x,y)$. The tomographic reconstruction problem to solve will then be to invert the Radon transform, *i.e.* find $f(x,y)$ given a set of measured projections $p_\theta(s)$. Tomographic reconstruction can be performed with analytical methods such as filtered backprojection (FBP). Analytical methods have, however, severe limitations, as it generally assumes that no image deteriorating factors are present, and therefore lacks the capability to compensate for these [18]. As a result, iterative reconstruction algorithms have been developed, where the estimate of the source distribution are refined in a series of repetitive calculations. These reconstruction methods are able to find solutions to a more general imaging model than the simple Radon transform stated above, and can also incorporate noise modeling [19]. Analytical and iterative reconstruction methods are discussed briefly in section 1.1.3 and 1.1.4, respectively.

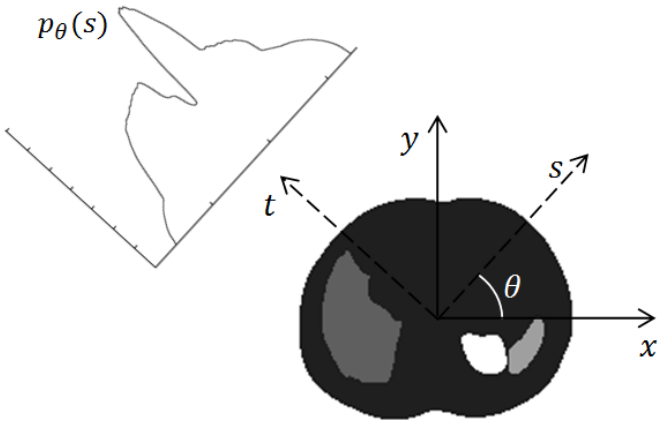

Figure 3: Illustration of ideal projection image acquisition, where the 1D projection $p_\theta(s)$ is formed by integrating the 2D source distribution $f(x,y)$ along the t-axis, according to Eq. 2.

1.1.3 Analytical reconstruction of tomographic images

The simplest and perhaps most intuitive approach to invert the Radon transform is the simple backprojection method, originally used for reconstruction of the first brain SPECT images in the 1960's [20]. In this method, the counts in each projection bin for each projection angle is uniformly spread over the line of response from the bin and summed. Mathematically, the backprojected image $b(x, y)$ is obtained by

$$b(x,y) = \int_0^{\pi} p_\theta(s) d\theta \qquad \text{Eq. 4}$$

which implies that for each coordinate (x, y) the appropriate value of $p_\theta(s)$ should be summed over all acquired projections. Since counts are being uniformly spread out along a projection line during backprojection, the reconstructed image will be a blurred version of the original distribution. It can be shown that the backprojected image and the original image are related by

$$B(\nu_x, \nu_y) = \frac{F(\nu_x, \nu_y)}{\nu} \qquad \text{Eq. 5}$$

where $B(\nu_x, \nu_y)$ and $F(\nu_x, \nu_y)$ are the 2D Fourier transform of $b(x, y)$ and $f(x, y)$ respectively, and $\nu = (\nu_x^2 + \nu_y^2)^{1/2}$ [21]. Eq. 5 suggests that the original image could be recovered by multiplying the Fourier transform of the backprojected image by a ramp filter ν. This is equivalent to multiplying the Fourier transform of each 1D projection with a 1D ramp filter, $|\nu_s|$ prior to backprojection. Filtered backprojection has been one of the most widely used reconstruction methods. The backprojected image $b_f(x, y)$ is calculated according to:

$$b_f(x,y) = \int_0^{\pi} \Im^{-1}[|\nu_s| \cdot P_\theta(\nu_s)] d\theta \qquad \text{Eq. 6}$$

where $\Im^{-1}$ denotes the 1D inverse Fourier transform and $P_\theta(\nu_s)$ is the 1D Fourier transform of $p_\theta(s)$. The use of a ramp filter generally leads to unacceptable noise amplification as the value of the filter function is monotonically increasing with increasing frequency. There can also be increased problems with 'streak' artifacts. For this reason, an additional filter, *e.g.* a Butterworth filter, is often employed to suppress the amplification of high frequencies. A SPECT slice reconstructed with simple backprojection and filtered backprojection with and without additional smoothing is shown in Figure 4 for comparison.

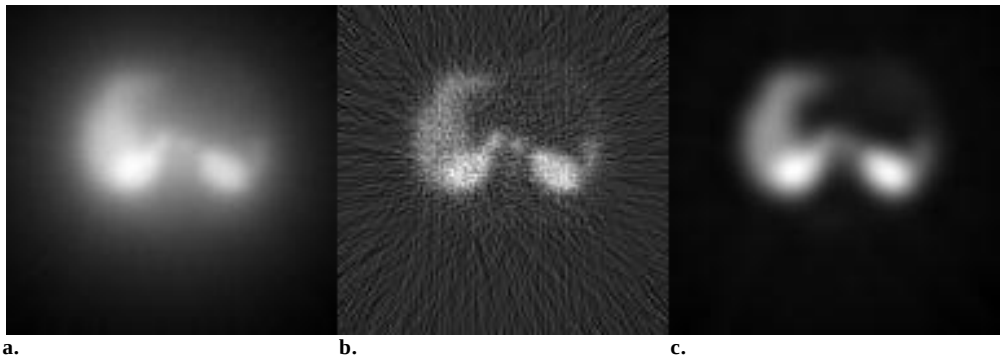

a. **b.** **c.**

Figure 4: Reconstructed SPECT slices with simple backprojection (a) filtered backprojection (b) and filtered backprojection with additional butterwort filtering prior to backprojection (c). The blurring in (a) is evident, (b) suffers from severe noise and streak artifacts, but image (c) has acceptable visual quality.

It is also worth to emphasize that the projections are constituted by a discrete set rather than a continuous function, which together with the presence of noise makes analytical solutions approximate at best. The major limitation of analytical reconstructions is however the oversimplified imaging modeled used, here represented by the Radon transform in Eq. 2 and 3, which assumes that no image deteriorating effects are present. A more realistic model would include effects of photon attenuation, scatter and the collimator-detector response. No analytical solutions exist for this complex problem to date, which has led to the development of iterative reconstruction algorithms [18].

1.1.4 Iterative reconstruction of tomographic images

As previously mentioned, iterative reconstruction methods can incorporate compensation for image deteriorating effects, such as attenuation and scatter. In addition, they can incorporate accurate noise modeling and provide reconstructed images with improved noise characteristics [19]. The major drawback compared to analytical reconstruction is the computation time, but recent hardware developments and accelerated reconstruction techniques have reduced this problem. Rather than describing the active distribution as continuous, as in Eq. 2 and Eq. 3, it can be considered to be discrete. In this case, the acquisition of projection images can be described by the equation

$$p_i = \sum_j a_{ij} f_j \qquad \text{Eq. 7}$$

where p_i is the measured count level in projection bin i, f_j is the count level in voxel j, and a_{ij} is the probability for a photon originating from voxel j to be detected in projection bin i. Eq. 7 can also be described as a matrix equation, where all elements a_{ij} constitute the transition matrix or system matrix **A**. This matrix is determined by the physics of nuclear medicine imaging, including factors such as attenuation, scatter and detector response.

Iterative reconstruction methods are designed to find the best possible estimate of the activity distribution, based on the measured projections. This is achieved by a setting a criterion that measures the goodness of the estimate, and designing an algorithm that finds an optimal solution, by a series of repetitive calculations, or 'iterations'. Numerous different reconstruction methods have been developed, with different assumptions of the underlying data. Radioactive decays are governed by Poisson statistics, suggesting that emission data is consistent with this distribution. This assumption led to the development of the Maximum-Likelihood Expectation-Maximization (ML-EM) algorithm [22, 23] which perhaps is the most common reconstruction algorithm for SPECT and PET today . The ML-EM algorithm can be described by the equation

$$f_j^n = \frac{f_j^{n-1}}{\sum_l a_{lj}} \sum_i a_{ij} \frac{p_i}{\sum_k a_{ik} f_k^{n-1}} \qquad \text{Eq. 8}$$

where f_j^n is the estimate of the source distribution after n iterations. The ML-EM reconstruction scheme is schematically illustrated in Figure 5.

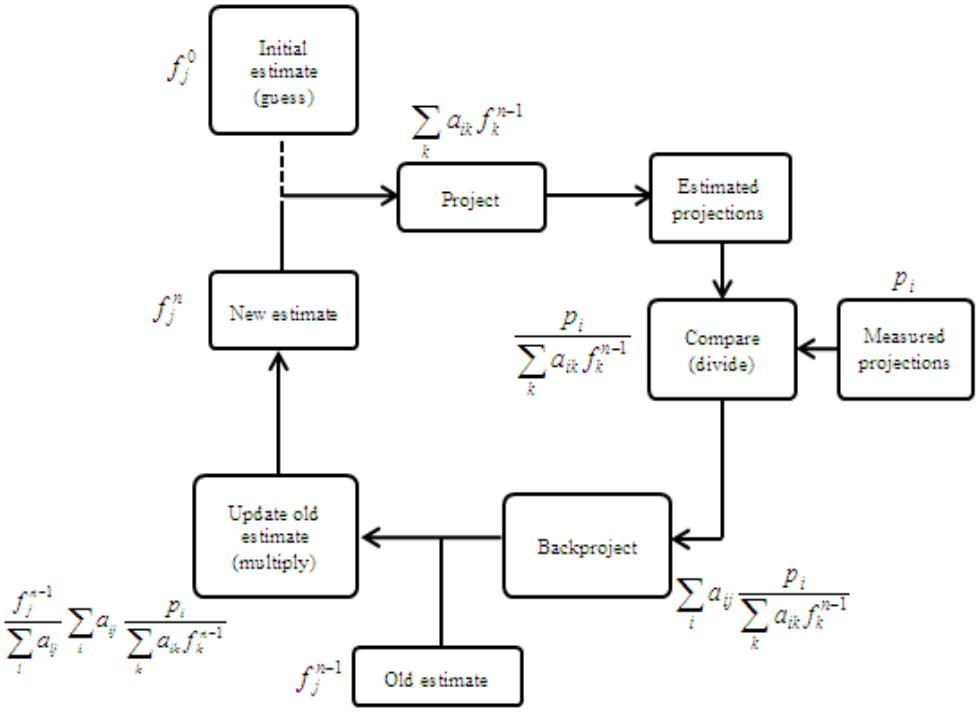

Figure 5: The ML-EM reconstruction scheme; schematic illustration of Eq. 8. See text for further explanation.

The ML-EM reconstruction method is computational demanding since it for general applications requires a large number of iterations (~30-50) [24], and different acceleration methods have been developed to decrease computation time. The most widely used is the Ordered-Subset Expectation-Maximization (OS-EM) algorithm [25]. It is essentially the same as ML-EM, but only uses a subset of all projections for updating the image estimate. This can mathematically be described as

$$f_j^n = \frac{f_j^{n-1}}{\sum_{l \in S_m} a_{lj}} \sum_{i \in S_m} a_{ij} \frac{p_i}{\sum_k a_{ik} f_k^{n-1}} \qquad \text{Eq. 9}$$

The number of subsets should be even and equal to the total number of projection angles divided by the number of projections in each subset. For instance, 60 projection angles can be divided into 10 subsets with 6 angles per subset. In this case, the image will be updated 10 times for each iteration, reducing reconstruction time significantly. Even though there is no theoretical proof that OS-EM converges to the same solution as ML-EM, there is virtually no differences in images of 'well-behaved' activity distributions that have been reconstructed with OS-EM compared to images reconstructed with ML-EM, provided subset size is chosen with some caution [19]. With increasing number of iterations, the likelihood increases which result in an activity estimate that is more likely to resemble the true distribution. But since a Poisson distribution is assumed, the resulting image will reflect the noisy distribution of emitted counts rather than the actual activity distribution, which is of main interest. The noise in the reconstructed image tends to increase with increasing number of iterations, which is why the reconstruction often is stopped at some pre-defined number of iterations. The convergence rate in iterative reconstruction has also been shown to be object dependent [26, 27] This means that the count level and resolution at different points in the reconstructed image is recovered at a different number of iterations, depending on the characteristics of the object, such as size, shape and count level in relation to the background.

1.2 Physical limitations and image quality in scintillation camera imaging

In section 1.1, image deteriorating effects such as attenuation, scatter and collimator-detector response were mentioned as a reason why the simple Radon transform and its analytical solutions are inadequate without explicit corrections for these effects. In this section, physical limitations of scintillation camera imaging and the impact on image quality will be discussed.

1.2.1 Photon attenuation

Attenuation is a generic term for all types of physical interaction between photons and matter. For normal tissue and photon energies representative for SPECT (~70-300 keV), the dominant mode of interaction is Compton scattering and photoelectric absorption. These processes lead to a decrease of primary photons, defined as detected photons that have passed through the body without interacting. The attenuation of the flux ϕ of primary photons as they pass through matter is described by

$$\phi = \phi_0 \cdot e^{-\left(\frac{\mu}{\rho}\right)\cdot\rho\cdot t} \qquad \text{Eq. 10}$$

where ϕ_0 is the initial flux, t and ρ is the thickness and density of the traversed material, respectively, and (μ/ρ) is the mass-attenuation coefficient that is dependent on material composition (Z) and photon energy $(h\nu)$. In scintillation camera imaging, where the activity distribution within in the body is of interest, attenuation is often considered to be an image degrading factor. This is due to the fact that photons originating from different locations within the body have to traverse tissue of different thickness and composition before reaching the detector, and the apparent activity distribution is hence distorted. This is most obvious for regions with variable density, *e.g.* close to the lung. For quantitative purposes, accurate attenuation correction is essential because the relation between counts and activity is often related by a single calibration factor. In SPECT, correction is often performed with a spatially co-registered 3D map of linear attenuation coefficients, which can be obtained by a CT-scan. This attenuation map can be used in an iterative reconstruction algorithm to compensate for the loss of primary photons due to attenuation.

1.2.2 Photon scatter

The decrease of the primary photon flux due to attenuation is accompanied by a build-up of secondary photons, that have been scattered one or several times in the object. Scattering of photons can also occur in the collimator, the surrounding materials, within the PMTs behind the crystal, *etc*. Coherent scattering is a process where an incident photon is scattered basically without energy loss. This process is often neglected because of the low cross section of interaction in tissue at photon energies used in nuclear medicine imaging. In addition, large scattering angles are unlikely since the differential cross section is strongly peaked in the forward direction. On the other hand, incoherent scattering, or Compton scattering, is the predominant mode of interaction. In this process, the incident photon interacts with an atomic electron and is scattered an angle θ relative to its original direction. In the interaction, a fraction of the original photon energy is transferred to the electron. The energy $h\nu'$ of the scattered photon is given by

$$h\nu' = \frac{h\nu}{1 + \frac{h\nu}{m_e c^2}(1 - \cos\theta)} \qquad \text{Eq. 11}$$

where $h\nu$ is the energy of the incident photon, m_e the rest mass of the electron and c is the speed of light. Eq. 11 is derived under the assumption that the electron is free and at rest.

Scattered photons are undesired since their apparent point of origin will be the last scattering point and not the emission site, resulting in images that do not represent the true activity distribution. This results in reduced image contrast and a slightly reduced spatial resolution. One could argue that scattered photons have less energy than primary photons and thereby could be easily excluded. However, scintillation cameras have relatively poor energy resolution, often in the vicinity of 10 % (FWHM of the photopeak) at 140 keV for a NaI(Tl) crystal. For this reason, the energy acceptance window has to be sufficiently wide in order to not exclude too many primary photons, and as a consequence a certain fraction of scattered photons will contribute to the acquired image.

1.2.3 Spatial resolution

The system spatial resolution of a scintillation camera is generally characterized by the point spread function (PSF), which is the system response when imaging a point source of activity in air, placed at a certain distance from the collimator face. The point spread function is often denoted the collimator-detector response function (CDRF), implying that it includes resolution effects due both to the geometric properties of the collimator and the properties of the crystal and detector itself. The abbreviations CDRF and PSF will be used interchangeably in this work. For a camera with a parallel-hole collimator, the PSF usually shows an approximately Gaussian shape and the width is given as the Full-Width at Half-Maximum (FWHM). The FWHM of the PSF for a typical scintillation camera system is approximately 1 cm at a source-to-collimator distance of 10 cm.

In the absence of septal penetration and collimator scatter, the point spread functions can be divided into two components, namely, the collimator geometric response and the crystal intrinsic response [28]. The geometric response function (GRF) of the collimator represents the probability distribution for a photon to pass through the collimator without interactions in, or penetration of, the collimator septa. The geometric response is determined by the characteristics of the collimator, *i.e.* the size (length and diameter) and shape of the holes and the septal thickness. For instance, a high-energy collimator usually has thick collimator septa to avoid septal penetration and the hole size must therefore be increased accordingly, to maintain a reasonable sensitivity. The GRF for a high-energy collimator is therefore generally wider then for a low-energy collimator. One important aspect of the GRF is the dependence of source-to collimator distance. This is illustrated in Figure 6. As the distance between the collimator and source of activity increases, the number of holes within the acceptance angle increases, resulting in a wider GRF. The GRF is often approximated as a Gaussian whose FWHM increases linearly with distance D;

$$FWHM(D) = a \cdot D + b \qquad \text{Eq. 12}$$

where a and b are collimator-specific constants, representing the resolution gradient and the resolution at the collimator face, respectively. By geometrical considerations, it can be shown that a is inversely proportional to the hole length, and that b is proportional to the hole diameter [29]. Because of the resulting distance-dependent spatial resolution, it is often desirable to minimize the distance between the patient and camera head during image acquisition, which is why modern camera systems often are equipped with systems that enable automatic detection of the body outline.

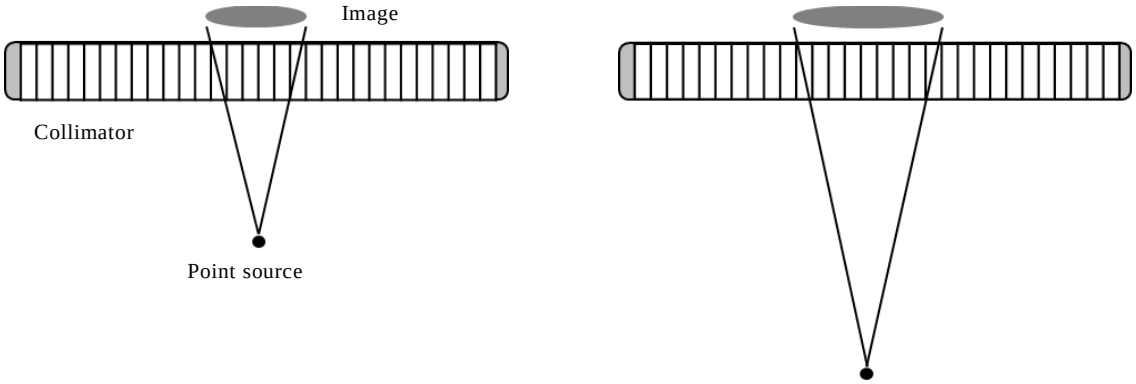

Figure 6: Schematic illustration of the distance dependent geometric response function (GRF). As the source-to-collimator distance increases, the number of collimator holes within the acceptance angle increases, and the GRF becomes wider.

The other component of the PSF is the intrinsic response function (IRF), which is defined as the response of the scintillation camera, without the collimator, to a pencil beam of impinging photons [28]. The production and collection of scintillation photons, as well as production of photo-electrons in the PMTs, are statistical processes and subjected to statistical noise, leading to uncertainty in the position estimation. Photons that undergo Compton scattering in the crystal also contributes to the finite intrinsic resolution, which is well modeled as a Gaussian function [17]. The intrinsic FWHM of a modern gamma camera is usually better than 4 mm but can have a spatial variation over the crystal because of variation in light collection efficiency [28]. This spatial variance is often not taken into account, which is a reasonable approximation since the GRF for most projection distances is the dominant component of the PSF. The IRF and GRF can be considered as two independent sources of blurring, and can therefore be combined into the point spread function by convolution. The convolution of two Gaussians remains a Gaussian function, and the resulting FWHM for the PSF as a function of distance is therefore well described by

$$FWHM(D) = \sqrt{(a \cdot D + b)^2 + c^2} \qquad \text{Eq. 13}$$

with c representing the FWHM of the IRF. This simple modeling of the point spread function is however not adequate in all situations. When imaging isotopes that emit high energy photons, *e.g.* ^{131}I, there is a significant contribution to the point spread function from photons that penetrate the collimator septa. The resulting PSF is in this case not radially symmetrical and other approaches for modeling are generally required.

1.2.4 Image noise

The physical processes involved in scintillation camera imaging are stochastic processes; the radioactive decay and emission of photons, the interaction between photons and matter and the detection process which involves production and collection of scintillation photons and generation of photoelectrons in the PMTs. For this reason, two identical measurements will not produce identical results. In terms of imaging, this measurement uncertainty appears as noise. In scintillation camera imaging, the probability of measuring exactly k counts in a pixel is given by a Poisson distribution with mean value λ;

$$p\{x = k\} = \frac{\lambda^k e^{-\lambda}}{k!} \quad \text{Eq. 14}$$

It can be shown that the mean count $\bar{x} = \lambda$ (for a large set of repeated measurements) and that $\sigma_x = \sqrt{\lambda}$, from which we can conclude that the local signal-to-noise ratio (SNR) at a given pixel is given by

$$\text{SNR} = \frac{\bar{x}}{\sigma_x} = \sqrt{\bar{x}} \quad \text{Eq. 15}$$

Eq. 15 states that it is desirable to maximize the number of collected photons during image acquisition to obtain the best possible image quality in terms of absence of noise.

1.2.5 Image contrast

Image contrast is a property of the image which makes two different objects distinguishable from each other. It can be assessed qualitatively by visual assessment or qualitatively for instance by calculating a normalized signal difference between an object and the background. The image contrast should not be confused with the object contrast, which in scintillation camera imaging is the true difference in activity concentration between two objects or an object and the background. A common way of describing the object contrast is the object-to-background activity concentration ratio (OBR). For quantitative measurements, the image contrast should be linear with the object contrast. The influence of photon attenuation, scatter, noise and imperfect resolution does however generally result in an image contrast different from the object contrast. Consider for instance two identical objects that lie below matter of different density. The difference in attenuation of photons emerging from the objects will generate a signal difference in the image, even though there is no object contrast. For this reason, it is important to correct for all image degrading factors in both quantitative and qualitative imaging.

2. Theory of the partial-volume effect

In SPECT (and PET) imaging, the image formation process results in a finite spatial resolution and thus a blurring of the activity distribution. As a consequence, activity from each point in the source distribution will be spread out over a volume in the reconstructed image. This can result in a distortion of apparent activity concentration and seriously affect the possibility for accurate quantitative analysis, as is demonstrated in Figure 7. Figure 7a represents the true source distribution whereas Figure 7b shows how this distribution would look in a typical emission tomography (ET) image. As can be seen, the count level in the high activity sphere will be underestimated because of spill-out to the surroundings. Similarly, the count level in the low activity sphere will be overestimated due to counts that have been spilled in from the background. Equilibrium of spill-in and spill-out will in this example only exist if the object and background have the same activity concentration. Spill-in and spill-out are not two different things; spill-in to structure *X* from structure *Y* is the same as spill-out from structure *Y* to structure *X*. Hence, the term spill-over is sometimes used for describing both these effects.

Besides the contamination of counts between the adjacent regions, the limited spatial resolution will also result in an underestimation of activity concentration for small objects even in the absence of background activity. A "small" object in this context is approximately smaller than 2-3 times the FWHM of the PSF. For larger objects, there will be full recovery of the signal in the central parts of the object. Obviously, the impact of the partial-volume effect is more prominent when small objects are of interest. This is demonstrated in Figure 8, where true and observed activity distributions for spheres of diameter 5, 10, 20 and 30 mm are shown. The resolution in the right image corresponds to a Gaussian FWHM of 10 mm. The smallest sphere is barely noticeable. Also shown are the corresponding profiles along the central row. It can be seen that the count recovery is not complete for the smaller spheres, and that the activity concentration in these object will be underestimated. For the 30 mm sphere, the count recovery is only complete in the innermost volume.

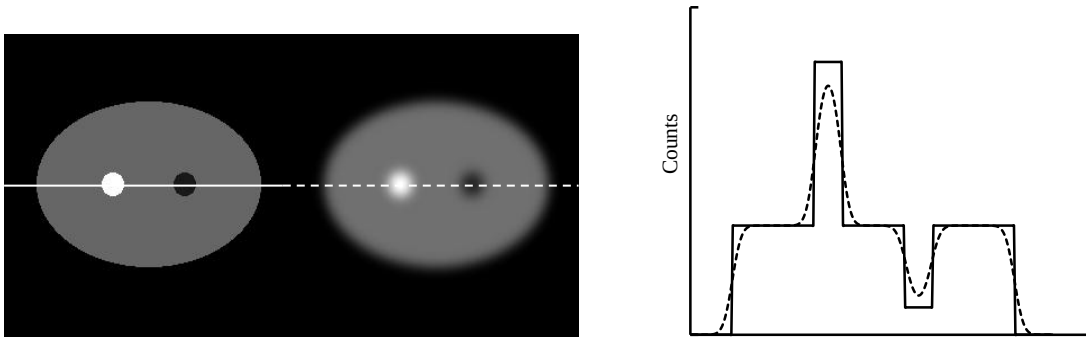

Figure 7: Illustration of effects of limited spatial resolution of a typical tomographic imaging system. The true source distribution is depicted in figure a., whereas figure b. shows a typical tomographic image of this object. The signal profiles along the central row have also been plotted. The apparent activity concentration in the spheres is distorted, due to spill-in and spill-out of counts from and to the background.

The spill-over and distortion of apparent activity concentration are called the partial-volume effect (PVE) [5-8, 17, 30-32]. This term usually also incorporates the discretization aspects, where one pixel or voxel contains different types of tissues. It would be more correct to refer to the blurring and spill-over of counts as spatial resolution effects, and reserve the term 'partial-volume' to the situation with tissue heterogeneity within one pixel or voxel. The naming convention is however relatively established, and PVE will therefore in this work be used for describing both the blurring and discretization aspect, with clarification when necessary.

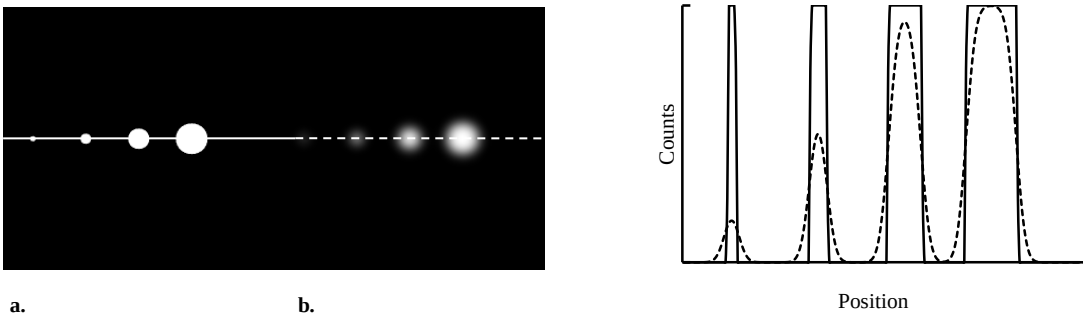

Figure 8: Illustration of the partial-volume effect and importance of object size. The true source distribution is depicted in figure a, whereas figure b shows a typical tomographic image of this object. The signal profiles along the central row have also been plotted. The sphere diameters are 5, 10, 20 and 30 mm, respectively, and the resolution corresponds to a Gaussian PSF with FWHM 10 mm. The maximum count level is recovered only for the largest sphere.

2.1 Existing PVC correction strategies

Several studies have showed that the PVE results in large bias in regional activity estimation, when using ET images for quantitative analysis [6, 11, 31]. As a result, different compensation methods have been proposed and developed. This section intends to give a brief overview of existing strategies for PVC in ET imaging, as given by Rousset *et al.* [5].

2.1.1 Partial-volume correction methods based on phantom measurements

One approach to compensate for PVE is to apply correction factors that have been derived from physical measurements. These measurements are often performed in standard geometries with simple geometrical shapes, such as spheres, cylinders or bars filled with activity. The correction factor is often in the form of a recovery coefficient (RC), which is defined as the ratio of measured activity to true activity in the object. Since PVE at first was considered as a problem for quantification of small high-activity objects in a low-activity background, recovery coefficients were measured and applied accordingly to compensate for spill-out. It became however obvious that the object-to-background ratio (OBR) had to be considered, in order to also correct for the counts that have been spilled in to the object from the background. This can be achieved by also utilizing a "cold spot recovery coefficient", defined as the ratio of measured activity concentration in the object to true background activity concentration, with OBR less than unity [33].

Correction methods based on physical measurements have some limitations, especially the fact that not all anatomical structures can be well approximated by simple geometrical shapes, and anatomical variability between different subjects is not easy to account for. The assumption that the image can be considered a two-component system with one target and one homogenous background structure is also not always valid. In addition to this, a large number of measurements have to be carried out to take all different combinations of object size, shape, OBR, radionuclide *etc.* into account.

2.1.2 Reconstruction-based partial-volume correction

The impact of the distance dependent resolution in SPECT, and thereby the PVE, can be diminished by incorporating explicit modeling of the PSF in the reconstruction algorithm [28, 34]. For instance, using a rotation-based projector-backprojector pair, the resolution modeling can be performed by convolving each plane parallel to the detector face in the current image estimate with the PSF corresponding to the specific distance between the image plane and detector face. Several studies have shown that resolution compensation methods in iterative reconstruction reduce PVE, but also that complete recovery of counts is generally not obtained [11, 32].

2.1.3 Partial-volume correction methods using anatomical information

Partial-volume correction can be performed with the aid of anatomical information, which today often is available by means of high-resolution CT or MRI. In addition, hybrid systems, such as SPECT/CT, have reduced the problem of spatial co-registration between functional and anatomical images when considering a single time-point measurement. These correction methods in general rely on segmentation of the anatomical image into different compartments, assumed to contain a uniform activity concentration. By modeling of the camera system's resolution properties, the magnitude of the spill-over between the different structures can be estimated and corrected for. Most published PVC methods based on anatomical information are post-processing methods, but anatomical information can also be utilized as a regularization within the iterative reconstruction methods to reduce PVE [35].

The PVC method implemented and evaluated in this work utilizes anatomical information and would thus sort under this category. It is a development of the template projection-reconstruction method which for SPECT was originally proposed by da Silva *et al*. [6]. In their studies, the method was evaluated in terms of absolute *in-vivo* quantification of regional myocardial activity uptake in a porcine model. A 3D volume of interest of the myocardial wall was outlined on CT images and used to create a template, which then was projected and reconstructed to obtain voxel-specific recovery coefficients for all voxels in the myocardium. Further development and evaluation of the method was presented by Du *et al.[11]* and Boening *et al. [8]* where the non-linearity of iterative reconstruction algorithms was accounted for by introducing perturbation based reconstruction of the templates. Development of a template-based PVC have also been published by Shcherbinin and Cellar [9, 36], using physical phantom experiments for validation in clinical realistic settings. Pretorius *et al.* introduced an additional parameter, the voxel filling fraction, to account for fractional presence of different structures within a single voxel, taking a step towards improving visual fidelity [7].

The template-based PVC method has in this work been adapted, further developed and evaluated for ^{177}Lu SPECT. A simple iterative scheme for calculation of count levels in structures affected by PVE has been developed, and the influence of different segmentation methods for generation of templates on quantitative accuracy has been investigated. In addition, an initial test of the method on clinical SPECT images has been performed.

3. Methods

The imaged-based correction method for the partial-volume effect used in this work is an adaption of the template projection-reconstruction method. The general idea behind this method is to create images of how the activity distribution is being distorted during the image formation process, *i.e.* the acquisition of projection images and reconstruction. These images can then be used to perform a partial-volume correction, by redistributing the counts in the reconstructed SPECT image. The method requires availability of a co-registered image with anatomical/structural information, such as a CT or a MR image of the object. The SPECT image itself can also be used as an anatomical map provided a distinct activity uptake in the organ of interest. The four main steps of the PVC method is schematically illustrated in Figure 9 and described in text (i-iv) below;

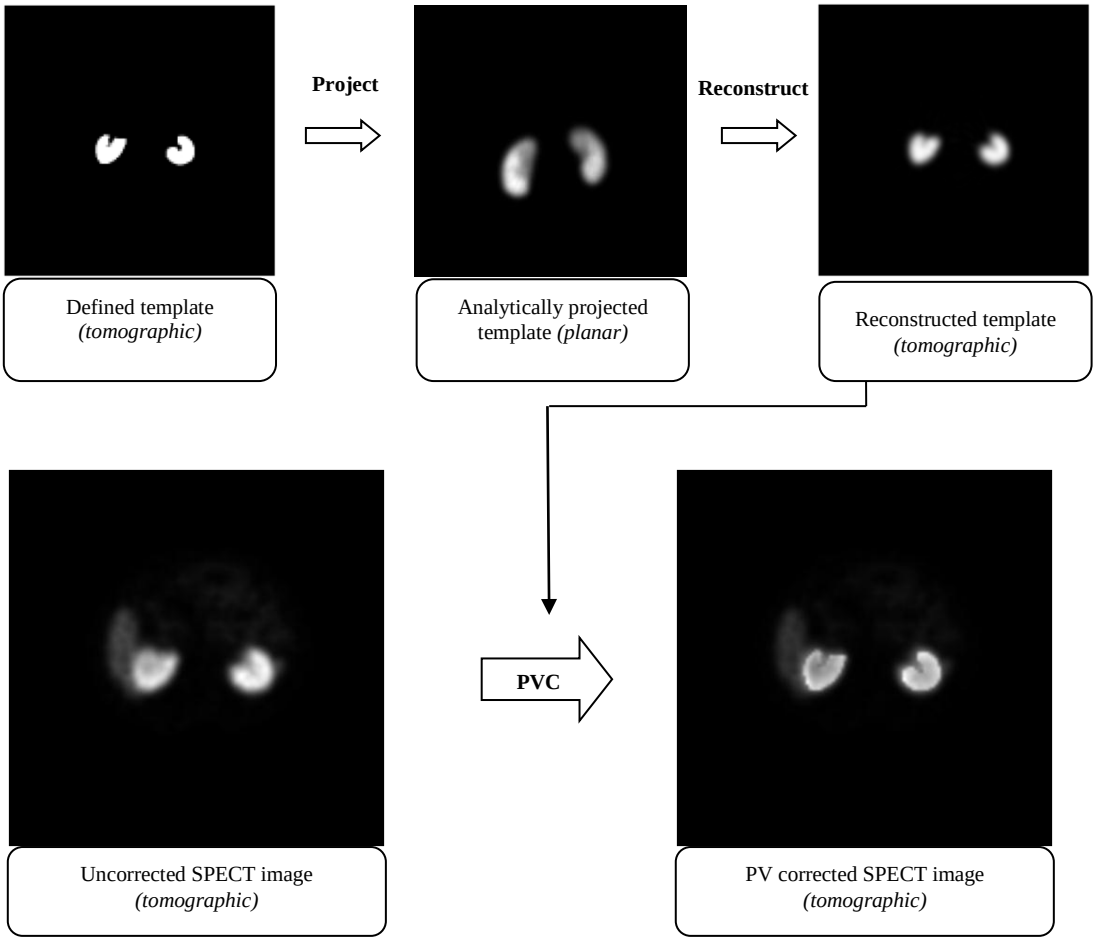

Figure 9: Schematic illustration of the steps involved in the partial-volume correction. The generated template is projected using a realistic model of the SPECT camera system. The reconstructed templates are essentially a map of voxel specific recovery coefficients, which can be used to correct the SPECT image for the partial-volume effect. In this example, all voxels within the kidney template have been corrected for spill-out only.

i) The organs/structures of interest are segmented on an anatomical image. For each structure of interest a *template* is the generated. The template is a binary image, where all voxels within that particular structure are assigned a value of unity and all other voxels a value of zero. The template will have a matrix size corresponding to that of the anatomical imaging system and should therefore be folded down to the matrix size of the SPECT image to be corrected. During resampling, it should be assured that the sum of all templates is unity for all voxels within the volume to be corrected. The number of segmented structures depends on the application, but should ideally be chosen so that each template represents a well-defined volume with a homogenous activity concentration.

ii) Each individual template is projected to a set of images corresponding to those acquired by the imaging system. Ideally, the characteristics of the imaging system and the projector should be identical. The projector should therefore accurately model all relevant physical processes and properties of the system, including attenuation and scatter as well as the collimator-detector response. The projection images can be calculated analytically or simulated using the Monte Carlo method. An analytical approach is however simpler in terms of computation time and practical usability.

iii) The projected templates are reconstructed, using the same reconstruction method and parameters used in the reconstruction of the SPECT image to be corrected. The result is a map of how the activity distribution within each structure has been spread out during the image formation process, *i.e.* acquisition of projection images and image reconstruction. It should be noted that this procedure implies that a uniform activity concentration within each segmented structure is assumed, and the segmentation of structures should be done to meet this criterion as well as possible.

iv) The reconstructed templates are subsequently used to perform a partial-volume correction for all voxels contained within the outlined structures. This is done by first subtracting counts that have been spilled over from adjacent regions, and thereafter dividing by the voxel specific recovery coefficient, *i.e.* the value of the reconstructed template, to compensate for counts that have been spilled out. In this work, an iterative method for PVC was developed, which reduces difficulties in evaluating mean count levels within the outlined structures. This is further described in detail in section 3.4.

3.1 Template generation

The template is a 3D image defining which voxels in the image volume that belongs to a specific structure. The creation of a template requires outlining of a volume of interest (VOI). This can be performed in different ways, for instance manually on a spatially co-registered anatomical image. Throughout this work, VOIs were outlined either by manual segmentation in SPECT or CT images, or by automatic segmentation in SPECT images. When working with some digital phantoms, such as the XCAT phantom described further below in the text, outlining is generally not necessary since the structures can be acquired directly from the phantom. The templates are subsequently created by assigning all voxels within a particular structure a value of unity, and all other voxels a value of zero. If the templates are available in high resolution, they have to be re-sampled to the SPECT voxel size before proceeding.

3.2 Analytical projection of templates

The templates were projected into sets of planar images using a rotation-based analytical projector, written in IDL [37] for this purpose. The projector was designed to model the distance dependent detector response as well as non-uniform photon attenuation based on a co-registered attenuation map. Modeling of scatter was not included in this work, mainly because of the complexity in modeling the spatially variant and object-dependent scatter response function. The impact of omitting scatter as a source of blurring will be discussed. The developed projector is schematically illustrated in Figure 10. For each projection angle, the image matrix volume is rotated so that the rows of the volume are parallel to the detector plane. The rotation is performed along the y-axis on a plane-by-plane basis using bilinear interpolation. Rotation error accumulation is avoided by performing all rotations starting from the original position and not the previous angle. Rotation based projectors are often used in reconstruction algorithms such as ML-EM or OS-EM [38, 39]. The rotation algorithm have been reported to be of importance in iterative reconstruction methods [40], but this has not been further considered.

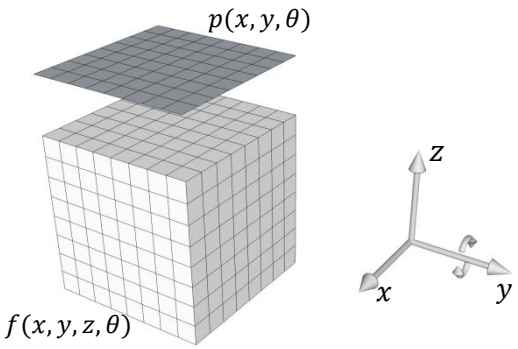

Figure 10: Schematic illustration of the analytical projector. The source distribution $f(x,y,z)$ is rotated so the x-y-planes are parallel to the detection plane for each projection angle. The projection images are formed by summing all pixels along the z-axis, with the possibility to include effects of attenuation and distance dependent resolution.

After rotation of the image matrix volume, the projection image $p(x,y,\theta)$for parallel beam geometry is calculated according to

$$p(x,y,\theta) = \sum_{z=0}^{z_{max}} f(x,y,z,\theta) \qquad \text{Eq. 16}$$

where $f(x,y,z,\theta)$ is the discretized source distribution after rotation θ degrees, x,y and z are the coordinate along the axis as depicted in Figure 10 and z_{max} is the plane closest to the detector.

Attenuation correction of the projection images is accomplished with a co-registered three-dimensional attenuation map which is rotated along with the source distribution. Let $\mu(x,y,z)$ be a 3D distribution of linear attenuation coefficients, rotated θ degrees from its original orientation. The accumulated attenuation matrix $\mathrm{M}(x,y,z,\theta)$ is the total attenuation factor for the counts originating from a given xy-plane and is calculated using a discretized version of Eq. 10;

$$\mathrm{M}(x,y,z,\theta) = \exp\left[-\sum_{z'=z}^{z_{max}} (\mu(x,y,z',\theta)) \cdot \Delta z\right] \qquad \text{Eq. 17}$$

where Δz is the pixel size in the z-direction. By attenuating each xy-plane with the appropriate attenuation matrix M, attenuated projection images can be calculated according to

$$p(x,y,\theta) = \sum_{z=0}^{z_{max}} [f(x,y,z,\theta) \cdot \mathrm{M}(x,y,z,\theta)] \quad \text{Eq. 18}$$

The distance dependent detector response was incorporated by means of convolution with the PSF of the imaging system being modeled. As previously described, the PSF is the combined effects of the collimator geometric response and the intrinsic spatial resolution. One advantage of using a rotation-based projector is that distance to the collimator face are the same for all voxels in a particular xy-plane and the PSF is therefore to a good approximation spatially shift-invariant in this plane. Each plane perpendicular to the z-axis in the image matrix volume is convolved with the spatially invariant PSF for the current distance to the collimator. By the convolution theorem, this is equivalent to a multiplication in the frequency domain. This approach is both intuitive and computationally efficient. Let $G\left(\nu_x, \nu_y, D(z)\right)$ be the 2D Fourier transform of the PSF over indices x and y at a given distance D for a given plane perpendicular to the z-axis;

$$G\left(\nu_x, \nu_y, D(z)\right) = \Im_{2D}[PSF(x,y,D(z)); x, y] \quad \text{Eq. 19}$$

and denote the 2D Fourier transform of the rotated source distribution for a fixed z over indices x and y with F;

$$F\left(\nu_x, \nu_y, z, \theta\right) = \Im_{2D}[f(x,y,z,\theta); x, y] \quad \text{Eq. 20}$$

The blurred count distribution for each plane z at the projection angle θ is obtained by taking the inverse 2D Fourier transform of the product of F and G;

$$f'(x,y,z,\theta) = \Im_{2D}^{-1}\left[\left(F\left(\nu_x, \nu_y, z, \theta\right) \cdot G\left(\nu_x, \nu_y, D(z)\right)\right); \nu_x, \nu_y\right] \quad \text{Eq. 21}$$

The resulting projection images with attenuation and point response modeling is given by

$$p(x,y,\theta) = \sum_{z=0}^{z_{max}} [f'(x,y,z,\theta) \cdot \mathrm{M}(x,y,z,\theta)] \quad \text{Eq. 22}$$

Obviously, blurred projection images without attenuation modeling can be calculated according to

$$p(x,y,\theta) = \sum_{z=0}^{z_{max}} f'(x,y,z,\theta) \quad \text{Eq. 23}$$

The projector was designed to create projection images with or without attenuation and distance-dependent blurring. To speed up the algorithm, only the planes where the source distributions are nonzero are included in the summation. The start angle, rotation direction and number of projections can be arbitrarily chosen. It was explicitly assured that no spatial shift is introduced by the convolution and that the center of rotation (COR) agrees with the COR of the reconstruction program. The projection distances D, here defined as the distance between the COR and collimator face, is determined for each projection angle from the spatially co-registered CT image, with an in-house written IDL routine described in section 3.2.2.

3.2.1 Simulations and verifications of the PSF

The hybrid imaging system of interest in this work for is a Discovery VH SPECT (General Electric, Milwaukee, Wisconsin) with a Hawkeye single slice CT unit. The SPECT camera has dual detector heads with 2.54 cm thick NaI(Tl) crystals and three different collimators optimized for low energy (*e.g.* $^{99}Tc^{m}$ imaging), medium energy (*e.g.* ^{177}Lu) and high energy (*e.g.* ^{131}I) respectively. The intrinsic resolution is 0.46 cm (FWHM) at 140 keV. The patient images used in this study have been acquired with the medium energy, general purpose (MEGP) collimator. The characteristics of the imaging system and the MEGP collimator have also been used in the Monte Carlo simulations of the digital XCAT phantom.

As been discussed previously, the projector should ideally be a perfect model of the imaging system. To obtain the Point Spread Function (PSF) for the GE Discovery SPECT system and the MEGP collimator used in clinical practice, simulations of a ^{177}Lu point source in air were carried out with the SIMIND Monte Carlo program [41]. The distance between the point source and the collimator face was varied between 0.5 and 40 cm. To investigate the importance of septal penetration and scatter in the collimator, simulations were made both with two different collimator routines. The first uses an analytical expression for the collimator response (routine 0), neglecting septal scatter and penetration, whereas the second (routine 1) performs actual ray tracing through the collimator [42]. Figure 11 shows the results of the simulations at source-to-collimator distance of 10 and 20 cm. A small broadening of the point spread function when collimator routine 1 is used can be noticed, especially at the larger distance. The effect of the hexagonal hole shape is also distinguishable, resulting in a PSF that is not perfectly radially symmetrical. The signal profiles along the middle row of the images can be seen in Figure 12 and 13. As can be seen, these profiles are well approximated by a Gaussian fit.

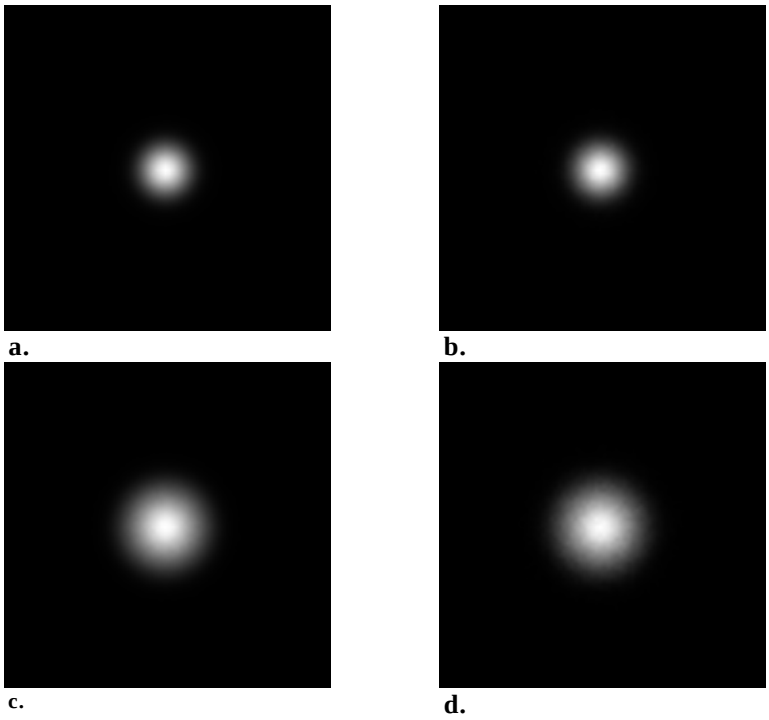

Figure 11: Left panel: Simulated PSFs with collimator routine 0 at 10 (a.) and 20 cm (c.) source-to-collimator distance. Right panel: Simulated PSFs with collimator routine 1 at 10 (b.) and 20 cm (d.) source-to-collimator distance. When routine 2 is used, the PSF shows a hexagonal shape because of the collimator design, and a small broadening can be seen due to septal penetration and scatter.

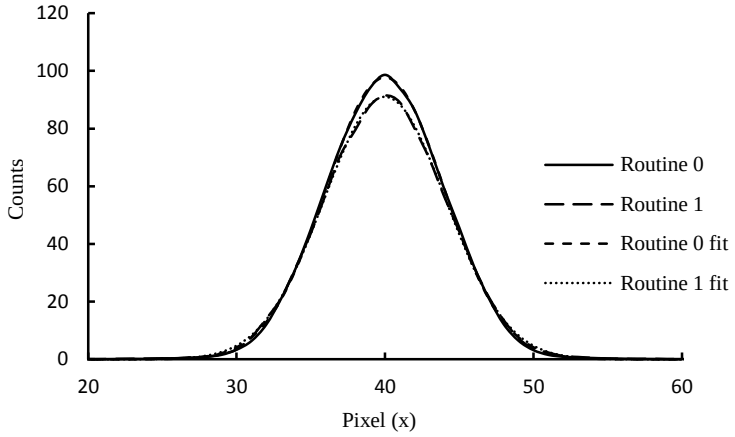

Figure 12: Line profiles along the central rows of images (a) and (b) in Figure 11. Gaussian curves have been fitted to the data with good agreement.

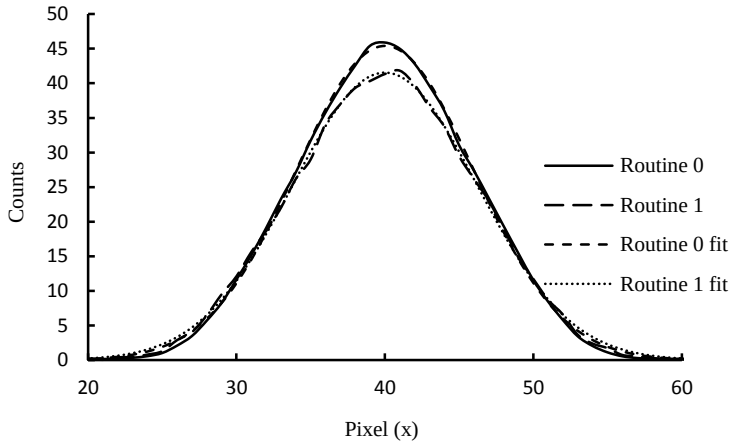

Figure 13: Line profiles along the central rows of images (c) and (d) in Figure 11. Gaussian curves have been fitted to the data with good agreement.

In the analytical projector previously described, it is desirable to describe the PSF as a function of depth. This was done by fitting a two-dimensional Gaussian to each simulated PSF by a non-linear least square fit. The average width (FWHM) in the x- and y-direction was then parameterized as a function of depth, by fitting the function given by Eq. 13 with *a*, *b* and *c* as fitting parameters. The obtained values of the FWHM as a function of distance is plotted in Figure 14 for both collimator routines. In terms of FWHM, septal penetration and scatter results in a slightly wider PSF, but the differences are subtle. The obtained values of the fitting parameters are given in Table 1.

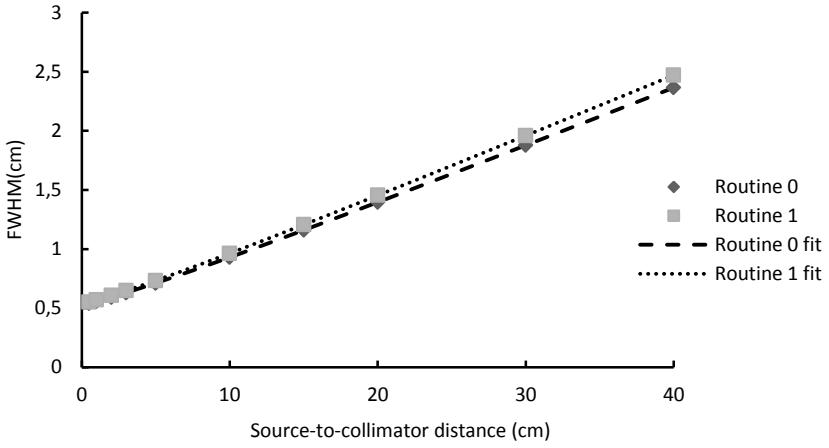

Figure 14: FWHM of the simulated point spread function for ^{177}Lu as a function of the distance between source and collimator for the two different collimator routines (see text).

Table 1: Value of fitting parameters for FWHM (cm) as a function of distance (cm) as given by Eq. 13.

Fitting parameter	Routine 0	Routine 1
a	0.049595	0.051967
b	0.349343	0.361593
c	0.388335	0.390838

When creating the template projections, the PSFs were approximated as rotationally symmetric Gaussians with FWHMs given by Eq. 13. In the XCAT phantom study, the projection images were simulated with collimator routine 0, and the fitting parameters obtained for routine 0 was therefore used to generate the PSFs. In the patient study, routine 1 was considered more appropriate in order to include the small broadening of the PSF due to septal penetration and scatter. It is however unlikely that the results would be different if this was omitted, since the effect is small, especially at small source-to-collimator distances. The difference becomes somewhat larger at greater distances, but the contribution to the image from photons emitted from larger distances will be smaller due to increased attenuation.

To verify SIMIND simulations of the GE Discovery VH system with the MEGP collimator, imaging of a small ^{57}Co point source positioned at different distances to the collimator were also performed and compared with corresponding simulations. ^{57}Co emits 122 keV gamma photons and septum penetration with a medium energy collimator is unlikely. A two-dimensional Gaussian was fitted to measured and simulated data and the average width in x- and y-direction was calculated and plotted as a function of source-to-collimator distance in Figure 15. The agreement between measured and simulated data is relatively good, and the two different collimator routines produce nearly identical results, as expected. Ideally, these measurements should have been performed with a ^{177}Lu point source since that is the radionuclide of interest for this application. However, the geometric response of the collimator, which is the most important component of the PSF, does not depend on photon energy in the absence of septal penetration. Since this effect appears to be of little importance for both nuclides with the MEGP collimator, the results suggests that the geometric response is accurately modeled by SIMIND. If this PVC method is to be used in clinical practice in the future, measurements of the PSF for the camera system should be made with ^{177}Lu to also verify the effects of intrinsic resolution, septal penetration and septal scatter for this nuclide.

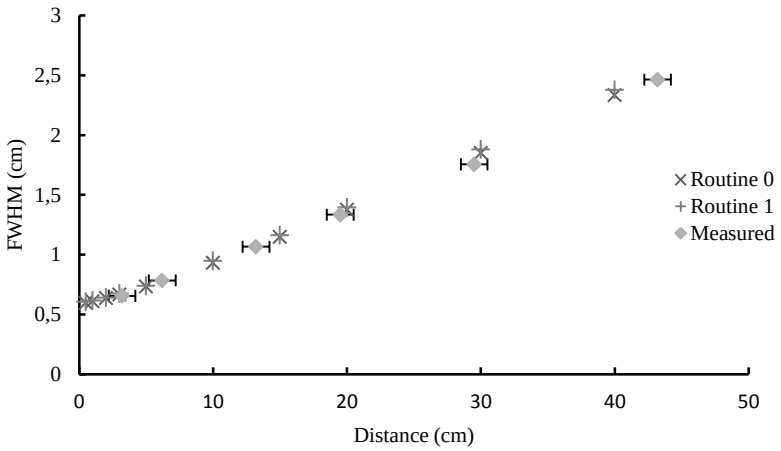

Figure 15: Width of Gaussian fit to measured and simulated point spread function for a ^{57}Co point source and GE Discovery VH system with MEGP collimator, as a function of distance between source and collimator face. The uncertainty bars on the horizontal scale are ± 1 cm (estimate) due to practical measurement difficulties.

3.2.2 Determination of projection distances

In order to convolve each plane in the image matrix volume with the appropriate PSF, the distance from each plane to the collimator face has to be known. If the detector head rotates with a fixed distance to the center of rotation (COR), this would be a trivial issue. However, in order to improve the resolution in the projection images, the detector heads on the GE Discovery VH system is set to follow the patient outline, made possible by sensors mounted on the camera heads. This means that the projection distance, here defined as the distance from the collimator face to the COR, is different for each projection angle. Unfortunately, the information on these distances for a given acquisition is not available from the clinical SPECT/CT-system. For this reason, an IDL routine was written to calculate these distances based on the co-registered CT image.

The steps included in the IDL procedure can be summarized as follows: In the IDL routine, the CT image is processed slice by slice. The images are first made binary, by setting a threshold value. All pixels with values above the threshold are assigned a value of unity while all other pixels are set to zero. An appropriate value is somewhere around 700 in Hounsfield units. For each projection angle, the binary image is rotated a corresponding number of degrees. The central column of the rotated image is then searched for an edge pixel. The edge pixel has a value of zero, and the sum of a certain number *n* of subsequent pixels in the column should exceed another threshold value *t*. The value of n and t can be adjusted to produce reasonable results, which could be assessed visually as illustrated in Figure 16. Since the pixel size is known, the distance between the edge pixels and COR can be calculated. The maximum distance for all slices is taken as the projection distance for each angle. An offset of 2 cm is added to account for the small distance between the camera head and patient during image acquisition. The projection distance array is saved and used as input in the analytical projector.

There are some limitations and sources of error that should be noted. Firstly, the field of view (FOV) of the CT image is not adequately large to include the arms in all slices, resulting in an underestimation of the distance to the COR for some angles due to the truncation. Secondly, the spatial extent of the camera head has not been taken into consideration. All points on the collimator face should be at least 2 cm from the body outline, and not just the central part as implicitly assumed with this approach. This is subject to future improvements. Despite the shortcomings, it is believed that this method produces more reliable results than if a constant distance to COR is assumed.

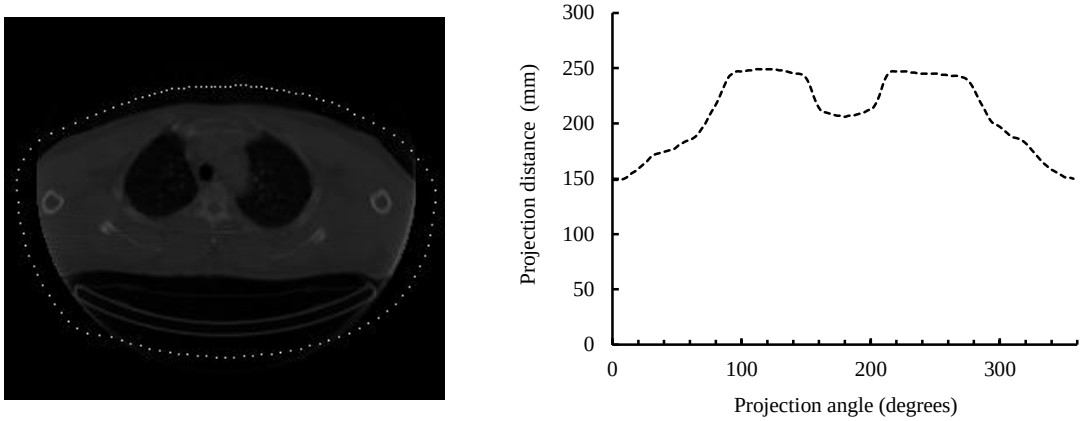

Figure 16: Determined projection distances for a single CT slice marked by the dotted line in the left image. The projection distance for a given angle is taken as the maximum distance for all slices. Note that the FOV of the CT is too small to include the arms in some slices, resulting in an underestimation of the distance for a few of the projections. This can be seen in the plot to the right, which shows the determined projection distance as a function of projection angle.

3.2.3 Attenuation maps

The discretized three-dimensional distribution of linear attenuation coefficients, used in the analytical projector as well as in the reconstruction program, was obtained by scaling the CT image in the patient study or by scaling of the density map from SIMIND in the simulation study. When simulating a SPECT study with SIMIND, a co-registered density map with the appropriate dimensions and pixel size is supplemented. CT images were converted to density map by the use of a bilinear calibration curve measured for the GE Hawkeye CT unit. The calibration curve is described by

$$\rho(x,y,z) = \begin{cases} 1017.4 + 1.033 \cdot H(x,y,z), & H < 51 \\ 1024.9 + 0.731 \cdot H(x,y,z), & H \geq 51 \end{cases} \qquad \text{Eq. 24}$$

where the density map $\rho(x,y,z)$is given in kg m^{-3} and $H(x,y,z)$ is the CT image in Hounsfield units, assuming $H = 0$ for water. The scaling from density to linear attenuation coefficients is performed by multiplying the value in each voxel by the mass attenuation coefficient for soft tissue or bone at the appropriate photon energy. All voxels with density exceeding 1200 kg m^{-3} are considered to contain cortical bone and all other voxels to contain soft tissue, with variable density. Mathematically, this can be written

$$\mu(x,y,z) = \begin{cases} \rho(x,y,z) \cdot \left(\frac{\mu}{\rho}\right)_{tissue}, & \rho < 1200 \\ \rho(x,y,z) \cdot \left(\frac{\mu}{\rho}\right)_{bone}, & \rho \geq 1200 \end{cases} \qquad \text{Eq. 25}$$

where (μ/ρ) denotes the mass attenuation coefficient at 208 keV. The value for the mass attenuation coefficient used was 0.1342 cm^2 g^{-1} and 0.1287 cm^2 g^{-1} for soft tissue and bone, respectively [43] .

3.3 Image reconstruction

All tomographic reconstruction of templates and SPECT images were made using an iterative OS-EM algorithm developed by Frey *et al.* [10], which utilizes a rotation-based projector, similar to the analytical projector developed in this work. It allows compensation for image degrading effects due to attenuation, scatter and collimator-detector response function (CDRF). The compensation for attenuation is based on the co-registered map of linear attenuation coefficients, obtained by mapping of CT images as described in section 3.2.2. Scatter correction in the reconstruction is performed by modeling the scatter contribution using the effective source scatter estimation (ESSE) method [44]. In this method, the effective scatter source is calculated by 3D convolution of the current estimate of the activity distribution and pre-calculated scatter kernels, weighted with the electron density obtained from a CT-image. The scatter component is subsequently calculated by forward projecting the effective scatter source. The projection operator of the scatter source should be identical to the one used for the primary source, and include attenuation and effects of the CDRF if this is to be corrected for in reconstruction.

All reconstructions were done using 10 or 20 iterations of the OS-EM algorithm with 10 angles per subset. Initially, 20 iterations were used but this number was reduced to 10 in the XCAT phantom study (described in section 4.2) to reduce image noise, when it was found that approximate convergence for all structures of interest was achieved already at 10 iterations (see Figure 17). The templates were reconstructed with correction for attenuation, but not for photon scatter, since only transport of primary photons was modeled in the analytical projector. The measured/simulated emission images were reconstructed with correction for both attenuation and scatter. Ideally, the reconstruction of templates and emission images should be done in the same way. However, since the projected templates consist of primary photons only, scatter compensation should not be employed. The possible effects of this inconsistency will be discussed. A 3D post-reconstruction Gaussian filter with a standard deviation of 1 pixel was employed to suppress noise and thereby improve visual quality of the reconstructed SPECT images. The perturbation-based method, described in section 3.3.1, was used for template reconstruction. One drawback of this method is that the reconstructed templates are subjected to noise which can reduce the accuracy of the PVC. The post-reconstruction low-pass filtering is thus important also for suppressing noise in the reconstructed templates, and the SPECT image to be corrected must be filtered accordingly.

Compensation for the CDRF in the reconstructions was not employed, since initial tests (not published here) showed that quantitative accuracy after PVC was not improved compared to the current method. In addition, more than 50 iterations was needed to reach convergence in the kidney VOI and the computation time for reconstructing the SPECT image and all templates was unreasonably long for practical purposes ,since a lot of reconstructions had to be performed to test the developed PVC method. The convergence rate is shown in Figure 17, where the mean number of counts as function of iteration number is plotted for the kidney VOI in one of the XCAT phantoms (t1) subsequently used for evaluation of the PVC method. An additional concern was the Gibbs-like ringing artifacts that arise when CDRF compensation is used in the reconstruction. The efficacy of CDRF compensation in terms of improving quantitative accuracy will be addressed in further studies.

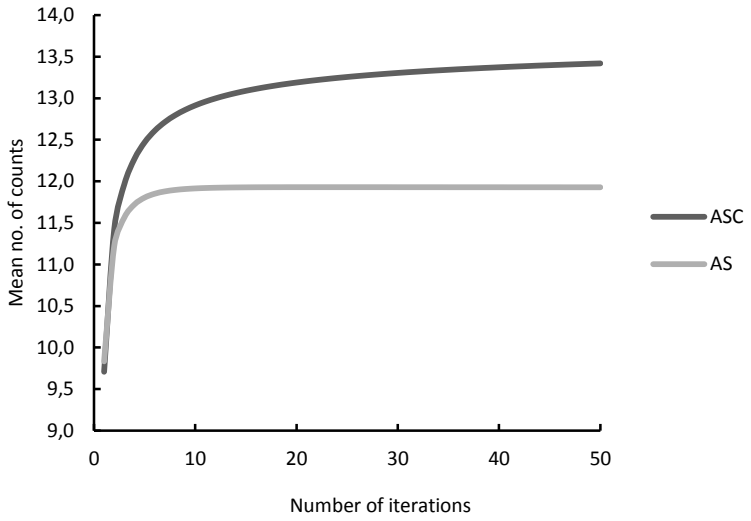

Figure 17: Mean number of counts as a function of iteration number in the kidney VOI of the XCAT phantom t1 used for evaluation of the PVC method. For reconstruction with compensation for attenuation and scatter ('AS'), convergence is reached after approximately 10 iterations. With compensation for attenuation, scatter and collimator-detector response ('ASC'), 50 iterations or more are required.

3.3.1 Pertubation-based reconstruction of templates

As previously discussed, the local convergence of iterative reconstruction methods is object-dependent. As a result, the local resolution in a reconstructed image depends on the characteristics of the object itself. This means that the resolution of the reconstructed templates depends on the shape and size of the template, which is an unwanted behavior since the blurring of templates should be consistent with the blurring of the SPECT image to be corrected. To account for this nonlinearity a perturbation-based reconstruction (PBR) was implemented [8, 11]. In this method, a combined projection set $\boldsymbol{p}$ (bold face characters denote a matrix) is created by adding the projected templates $\boldsymbol{t}$ as a small perturbation to the measured emission set $\boldsymbol{m}$;

$$\boldsymbol{p} = \boldsymbol{m} + \delta \boldsymbol{t} \qquad \text{Eq. 26}$$

with $\delta = \max(\boldsymbol{m}) / \max(\boldsymbol{t}) \cdot p$, where p is the perturbation factor. The exact value of p is not critical, but should be small enough to assure that the contribution of the templates is sufficiently small to not affect the reconstruction. It has been shown that values of p between 0.0001 and 0.1 give similar results [11]. Throughout this work, a perturbation factor of 0.01 was therefore used. Reconstruction of the measured and combined projection set is the performed to obtain the tomographic images $\boldsymbol{M}$ and $\boldsymbol{P}$, respectively. The reconstructed templates $\boldsymbol{T}$ is then obtained by subtracting $\boldsymbol{M}$ from $\boldsymbol{P}$ and scaling back to original count level according to

$$\boldsymbol{T} = \frac{\boldsymbol{P} - \boldsymbol{M}}{\delta} \qquad \text{Eq. 27}$$

With this approach, the resolution degrading effect of the reconstruction process is more similar on the templates and on the SPECT image, than what would be the case by direct reconstruction of $\boldsymbol{t}$. The perturbation method has, however, some disadvantages compared to direct reconstruction. The measured emission set is subjected to noise and non-uniform count distribution which will propagate to the reconstructed templates. It is therefore not unlikely that the PVC method could be more sensitive to noise with PBR. The noise sensitivity of the method has been investigated and will be further discussed in this dissertation.

3.4 Development of an iterative PVC algorithm

The reconstructed templates are used to perform the partial-volume correction, i.e. correct for spill-in and spill-out of counts between all pre-defined structures. The correction algorithm is, in the ideal case, simply a redistribution of counts determined by the spatial extent of the reconstructed templates, and should not affect the total number of counts in the image. For each structure X, the spill-in contribution from the other defined structures Y is subtracted from each voxel V_j by

$$C_{SI}(V_j) = C(V_j) - \sum_Y T_Y(V_j) \cdot \bar{C}_Y \qquad \text{Eq. 28}$$

where $C_{SI}(V_j)$ is the spill-in corrected count, $C(V_j)$ is the uncorrected count, $T_Y(V_j)$ is the value of the reconstructed template for structure Y in voxel V_j and $\bar{C}_Y$ is the mean count level in structure Y. It should be noted that the correction is only valid of the segmented structures Y represent volumes with a homogenous count distribution. The correction for spill-out from voxels within structure X is then performed by dividing with the voxel specific recovery coefficients, *i.e.* the value of the reconstructed template T_X;

$$C_{PVC}(V_j) = \frac{C_{SI}(V_j)}{T_X(V_j)} \qquad \text{Eq. 29}$$

where $C_{PVC}(V_j)$ is the partial-volume corrected count level in voxel V_j. The partial-volume correction is performed for all voxels contained in the segmented structures. Consider for instance that templates for the liver, spleen, kidneys and a rest-of-body have been generated. When correcting voxel within the liver, the residual structures Y represent the spleen, the kidneys and the rest-of-body, which contribute to spill-in to the liver (structure X). When correcting voxels within the kidneys, the residual structures Y are the liver, spleen and rest-of-body. Correcting voxels within the spleen and rest-of-body templates are performed in the same manner. A modification of Eq. 29 can be made if the templates are available in higher resolution (smaller voxels) than the SPECT image, for instance if the outlining of structures are made on a high resolution CT image. In the SPECT image there will be edge voxels, containing two or more different types of tissue. This is also known as partial-volume, but is an effect of the discretization and finite pixel size rather than the spatial resolution of the system. The correction method described above explicitly assumes that a voxels is completely within or outside a structure, leading to an over- or under-compensation of the edge voxels. To account for this, the *voxel filling fraction* F, originally proposed by Pretorius *et al.* [7], can be incorporated. The second step of the partial- volume correction is then instead performed according to

$$C_{PVC}(V_j) = F_X(V_j) \cdot \frac{C_{SI}(V_j)}{T_X(V_j)} \qquad \text{Eq. 30}$$

The voxel filling fraction $F_X(V_j)$ has a value of unity when V_j is completely in the structure X and less when only partially in X. The image F can be obtained by resampling the high resolution template with bilinear or cubic interpolation, allowing for pixel values between 0 and 1. The incorporation of the voxel filling fraction only affects the edge voxels and is therefore not critical for quantification of counts within a VOI. It does however improve the visual quality of the partial-volume corrected image, which will be demonstrated later.

When performing the first part of the PVC as described by Eq. 28, an accurate estimate of the mean count $\bar{C}_Y$ is necessary. For large structures, the count level can be evaluated far away from any edges, *i.e.* where $T_Y \approx 1$, to avoid regions with diminished counts due to spill-out. This is not possible for smaller structures where the count recovery in the entire structure is incomplete. In these cases, $\bar{C}_Y$ will be underestimated, and therefore also the calculated spill-in contribution to structure X. One could start by apply a recovery compensation for the small regions, but this

would result in an overestimation of A_Y since spilled-in counts have not been subtracted. To overcome these issues, a simple iterative method to refine the estimates of $\bar{C}_Y$ was developed. In this method, the PVC is first applied with initial values of $\bar{C}_Y$ evaluated over the entire structure in the original SPECT image. New values of $\bar{C}_Y$ are then calculated as the mean number of counts in the different structures of the PV corrected image, and the correction is subsequent applied again on the original image after which new values of $\bar{C}_Y$ can be calculated. This process is then repeated for a number of iterations. It should be emphasized that the correction itself is not performed in an iterative manner. The purpose of the iterative procedure is only the refine the estimates of $\bar{C}_Y$ and the final PVC is always performed on the original uncorrected SPECT image.

For some voxels the subtraction in Eq. 28 will result in negative values due to i) heterogeneous count distribution within the defined templates, ii) imperfect match between the projector and the imaging system, iii) possible spatial mismatch between the template and the SPECT image and iv) the presence of noise. Negative values in a SPECT image have no physical meaning and voxels with negative values are therefore assigned a value of zero prior to the final evaluation of the corrected image, but not as a part of the iterative algorithm. This truncation may introduce some bias with regards to total count number after correction as compared to the total count number in the uncorrected image, but this has not been further considered.

4. Evaluation and experiments

A series of tests was performed to evaluate the different components of the developed method and to assure its functionality from a practical point of view. The iterative PVC method was tested under perfect conditions with a digital geometrical phantom. The same phantom was used to investigate the influence of noise and compare the perturbation based method with direct reconstruction of templates. A Monte Carlo simulation study with the digital extended patient-realistic cardiac-torso phantom (XCAT) [12, 13] was carried out to evaluate the method under more clinical conditions. Finally, the PVC method was applied on existing clinical images of real patients.

4.1 Evaluation of the iterative PVC algorithm

A voxel based geometrical phantom was created to study best possible performance of the iterative PVC method, with a perfect match between the projector and imaging system and in absence of scatter and noise.

The phantom consisted of three spheres of different sizes in a uniform elliptical cylinder, as can be seen in Figure 18. The long- and short-axis of the elliptical cylinder was approximately 221 and 161 mm, and the cylinder length was 514 mm. The volume of the spheres was 4, 34 and 530 cm^3, respectively, and the sphere-to-background activity concentration ratio was defined to 5:1. The corresponding density map was the elliptical cylinder without the spheres, with density 1.0 g cm^{-3}. The matrix size used was 256x256x128 with voxel size 2.01x2.01x4.02 mm^3. This matrix and voxel size was chosen for simplicity since it corresponds to the matrix size used for clinical imaging with the GE Millennium SPECT/CT unit. Templates for each sphere and the background volume were also generated, with guaranteed perfect alignment to the source map.

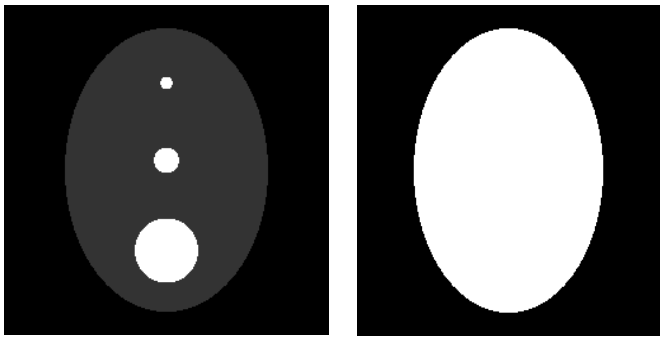

Figure 18: Central slice of the geometrical voxel phantom (a) and density map (b). The sphere volumes are approximately 4, 34 and 530 cm^3, respectively and the object-to-background activity ratio was 5:1.

The source map, density map and templates were folded down to 128x128x128 using bilinear interpolation. The source map and templates were then projected into 60 projection images of matrix size 128x128, including effects of attenuation and collimator-detector response, with the analytical projector, as has been described in section 3.2. The density map was rescaled to linear attenuation coefficients by multiplication with the mass attenuation coefficient for soft tissue as given by Eq. 25. The projection images of the source distribution and the templates were reconstructed using OS-EM with 20 iterations and 10 angles per subset, including correction for attenuation and post reconstruction filtering as described in section 3.3. The templates were reconstructed both directly and with PBR to study qualitative and quantitative differences. PVC of the SPECT image was performed using 5 iterations of the iterative PVC algorithm.

The mean count level for the background and each sphere was evaluated for the images with and without PVC, and the error ε was calculated according to

$$\varepsilon = \frac{\bar{C}_X - \bar{C}_X^{true}}{\bar{C}_X^{true}} \quad \text{Eq. 31}$$

where $\bar{C}_X$ is the measured mean count level and $\bar{C}_X^{true}$ is the mean count for the true source distribution. The mean value was calculated only where F_X = 1 to only include voxels fully within the VOI, thereby avoiding issues of structure heterogeneity within voxels.

4.1.1 Noise sensitivity

An additional test was performed to investigate the noise sensitivity of the method, and study PBR as compared to direct reconstruction (DR) of templates under the influence of noise. Poisson noise corresponding to a total count number of 1,5,10 and 50 million counts was added to the projections of the source distribution, prior to reconstruction. The quantitative error in mean count level was then evaluated before and after PVC as given by Eq. 31 as a function of noise level.

4.2 XCAT phantom study

The main purpose of this study was to examine the potential of the developed PVC method under more realistic conditions than in the studies with the geometrical phantom. In this study, the source distribution is clinically more relevant and the projection images are more realistic, especially since they include scattered photons. The digital extended cardiac-torso phantom (XCAT) [12, 13] was used to create source distributions and density maps of a normal-sized male, used as input in a SPECT study Monte Carlo simulation. The phantoms were generated in 350 axial 2 mm thick slices from the neck to lower pelvis. The matrix size was 256x256 with pixel size of 2 mm. The relative activity concentrations in the different organs were set to resemble a representative patient being treated with ^{177}Lu-Tyr3-Octreotate at four specific times post injection, based on data from literature [45-47] as well as from 25 patients in the Oncology Department at Skåne University Hospital in Lund. Initially, phantoms with relative complex activity distributions were generated, with specific activity concentrations defined for the blood pool, intestines, kidney cortex, kidney medulla, spleen, liver and lungs to get a good visual resemblance between simulated and clinical images. These phantoms where however not used for evaluation of the developed PVC method, mainly because of difficulties in determining which voxels belong to a certain structure. For instance, the kidneys as they would be outlined by an operator would consist of a mixture of renal cortex, medulla, pelvis and blood vessels and the "true" activity concentration in the VOI is hence not known. Simplified versions of the phantom were therefore generated, without blood vessels and activity concentrations only defined for kidneys (identical values for cortex, medulla and pelvis), liver, spleen and remainder of body.

An example of activity distribution and corresponding density map generated by the XCAT software is shown in Figure 19. The relative activity concentrations in the different compartments of the phantoms are given in Table 2. Note that the values are only comparable for a specific time post-injection, since they are normalized to a kidney activity concentration of 100.

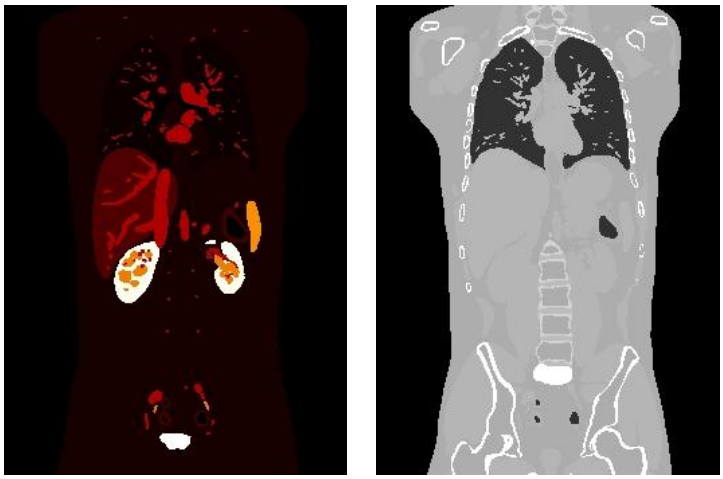

a. **b.**

Figure 19: Example of coronal slice of the activity distribution (a) and density map (b) generated by the XCAT phantom software. The activity distribution has been set to correspond to a patient undergoing treatment with ^{177}Lu-Octreotate, approximately 1 h post injection.

Table 2: Relative activity concentrations in different organs and at different times post injection for the male XCAT phantom, normalized to 100 for the kidney cortex at each time.

Organ/Structure	Approximate time p.i.(h)			
	0.5	24	96	168
Kidney	100	100	100	100
Spleen	79	133	145	164
Liver	25	26	32	43
Remainder	7	2	1	1

The generated phantoms were used as source and density maps in SIMIND to simulate a SPECT study, matching the GE Discovery SPECT system and clinical circumstances as close as possible. The most relevant simulation parameters have been summarized in Table 3. The simulations were performed with enough photon histories to create virtually noiseless projections. Poisson noise was then added, corresponding to a total count number of 15 million over all projections. This noise level was arrived at after studying count levels in a number of clinical images.

Templates were generated for the liver, spleen, kidneys and rest-of-body. The liver and spleen was included because of the high activity uptake and proximity to the kidneys, and hence possibility for a significant spill-over contribution. This is also a reasonable approach from a practical viewpoint since these organs are relatively easily distinguishable in CT images. The structures were not manually outlined but acquired directly from the XCAT phantom. The templates were thus available in higher resolution (2 mm voxels), allowing for PVC incorporating the voxel filling fraction as given in Eq. 30. The kidneys were also outlined by automatic segmentation on the SPECT image, using a method based on Fourier descriptors developed by Gustafsson [48]. This is a method that is intended to be used on clinical images, and represents a more realistic scenario where the template and true source distribution are not perfectly spatially aligned. In this case, the templates were only available with 4 mm voxel size, and only available as binary images, *i.e.* only containing values of 0 and 1. Therefore, the second part of the PVC was performed according to Eq. 29. It should be noted that the templates for the spleen and liver was in both cases generated directly from the organ configuration in the phantom, as the automatic segmentation method is currently only working satisfying for the kidneys. The spleen and liver templates was however manipulated to assure that there was no overlap with the kidneys.

Table 3: Summary of parameters used in SIMIND for simulation of ^{177}Lu SPECT imaging with the GE Discovery SPECT system.

General		
	Crystal	1“ (2.54 cm) NaI(Tl)
	Intrinsic spatial resolution	4.6 mm FWHM at 140 keV
	Energy resolution	9.5 % at 140 keV
	Backscatter material	8 cm Lucite
Collimator		
	Type	MEGP (parallel hole)
	Hole shape	Hexagonal
	Hole diameter	3.00 mm (F2F)
	Septal thickness	1.05 mm
	Hole length	58.0 mm
	Collimator Routine	0 (analytical)
Acquisition parameters		
	Number of projections	60
	Rotational extent	360°
	Matrix size	128 x 128
	Pixel size	4 mm
	Energy window	208 keV ± 10 %
	Automatic body contouring	Yes, offset 2 cm

The templates were projected into sets of 60 projection images with the analytical projector described in section 3.2, using the same acquisition parameters as in the simulation. The projection distances were determined with the in-house written routine described previously, using the co-registered density map obtained from SIMIND. This density map is identical to the one used in the simulation, but resampled to match the matrix size and dimensions of the acquired projection images. Reconstruction was performed with 10 iterations of OS-EM and post-reconstruction filtering as described previously. The SPECT image was reconstructed with compensation for attenuation and scatter whereas the templates were reconstructed with compensation for attenuation only, since the analytical projector used for the templates only models transport of primary photons. Since the PBR method was used for reconstructing the templates, another SPECT image without scatter correction was also reconstructed. This image was however only reconstructed to calculate the templates as given by Eq. 27 and was then discarded.

PVC was performed with 5 iterations of the iterative algorithm, and the quantitative accuracy before and after PVC was evaluated by calculating a mean error ε as in Eq. 31, comparing the measured mean activity concentration within the liver, spleen and kidneys with the true activity concentration used in the simulation. A total correction factor k, defined as the ratio of activity concentration after PVC to the activity concentration without correction, was also calculated for each organ. Since the raw data in the reconstructed SPECT image is in units of counts/voxel, the data must be scaled to activity per unit volume before comparison can be made. The system sensitivity, 9.51 counts per second (cps) and MBq, had been previously determined by simulation of a measurement with a small, infinitely thin, Petri dish-like source with uniformly distributed activity. The radius of the dish was 5 cm, and it was positioned 10 cm from the lower collimator surface. The simulation was conducted using the same setting for the camera parameters (energy window, collimator and energy resolution) as for the XCAT simulation. The septal penetration was confirmed to be very small and was therefore assumed negligible.

4.3 Test on clinical images

The developed method was also applied on existing patient images to verify the robustness of the method and investigate if the results were consistent with the results obtained in the phantom study. An additional purpose was to compare quantitative values obtained after PVC with values obtained with the standard protocol currently in use for clinical dosimetry. In this protocol, the PVE is reduced by utilizing CDRF compensation in reconstruction, and by intentionally excluding the outer rim of the organs which is known to be affected by PVE when manually outlining VOIs, instead of following the anatomical outlines as they appear in the CT image.

Images from 2 different patients with 2 therapy sessions each were used for this evaluation. All projection images had been acquisitioned approximately 24 h post injection of activity, and CT-scans had also been performed. The projection images were acquired at 60 projection angles with 360 degrees extent of rotation. The matrix size was 128x128 with a pixel size of 4.02 mm, whereas the pixel size in the CT image was 2.01 mm. The acquisition time was 45 seconds for each angle, and he total number of counts was between $6.4 \cdot 10^6$ and $8.2 \cdot 10^6$ for all images. The energy acceptance window was 208 keV±10 %.

To study the dependence of the method on the outlining of structures, three different methods for outlining of the kidney VOI were employed; manual outlining on the CT image (Method 1), automatic segmentation of the SPECT image (Method 2), and using the previously outlined kidney VOIs used for activity quantification in the standard clinical protocol (Method 3). The outlining of kidney VOIs for method 3 were performed manually on fused SPECT/CT images. Since the GE Discovery VH/Hawkeye hybrid SPECT/CT system was used for image acquisition, accurate spatial co-registration between SPECT and CT images is assured. It should be emphasized that the VOI is used both to create the template and define the voxels which are included in quantitative evaluation. An example of a template for the left kidney generated by these three methods is shown in Figure 20. It is evident that they are not equivalent. The automatic method (2) produces smooth volumes but is not able to produce the concave shape in the indented region where the renal pelvis is attached. Compared to the VOI outlined on the CT image (method 1), they are slightly smaller. The VOI outlined using the standard protocol (method 3) does not resemble the anatomical appearance of a kidney, and the volume is largely underestimated. The reason for the small VOIs using method 3 is that the PVE is supposed to be implicitly corrected or by avoiding the organ edges. For instance, the calculated volume for the templates, shown below, are 164, 137 and 79 cm^3 for method 1, 2 and 3, respectively. It should be noted that the manual outlining on the CT image was performed by a relatively inexperienced operator, whereas the operator responsible for drawing VOIs for clinical evaluation was considerably more experienced. In all three cases, templates for the liver and spleen were generated by using VOIs that had been manually outlined on a fused SPECT/CT image by the experienced operator, with purpose of activity quantification. A similar underestimation of volume is hence expected also for these organs. The rest-of-body template was generated with an in-house written routine based on a region-growing method.

All templates were projected into 60 angular views with the analytical projector, including effects of attenuation and distance-dependent resolution. Projection distances were determined with the CT image and the in-house written routine described previously. The CT image was rescaled to linear attenuation coefficients according to Eq. 24 and Eq. 25 for attenuation calculations in the projector and for attenuation correction in reconstruction. Reconstruction was performed with 20 iterations of the OS-EM algorithm, and using PBR for the templates. The SPECT image was reconstructed with corrections for attenuation and scatter, and templates only with correction for attenuation, in the same manner as in the XCAT phantom study. The reconstructed templates were used to perform the PVC, which was carried out with 5 iterations of the PVC algorithm described in section 3.4. The mean number of counts within the VOI used for generation of templates was evaluated before and after correction, and the correction factor k, defined as previously, was calculated.

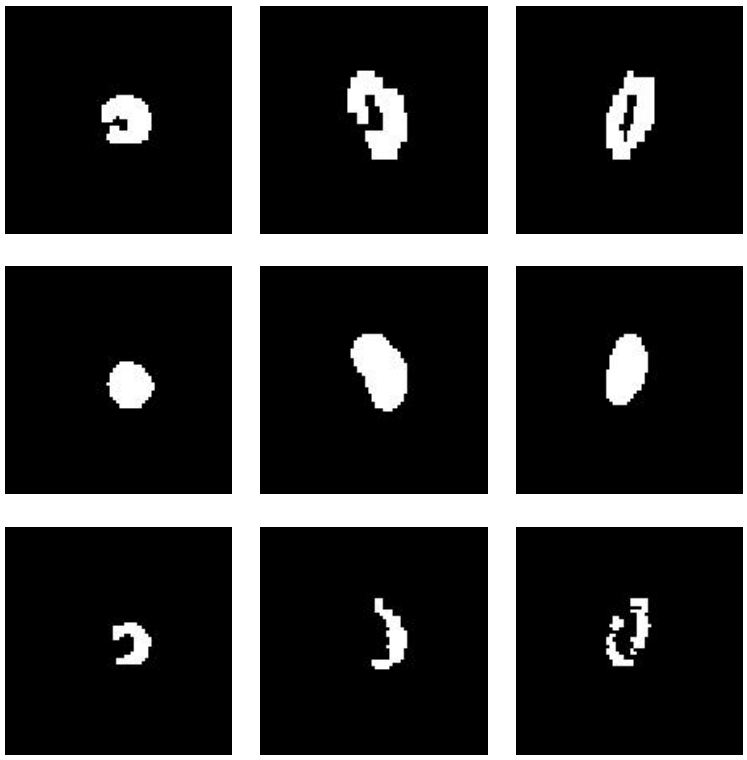

Figure 20: Transversal (left column), coronal (middle column) and sagittal (right column) slices of a left kidney template generated by manual outlining in a CT image (Method 1, top row), automatic segmentation of a SPECT image (Method 2, middle row) and by previously outlined kidney VOI used for activity quantification (Method 3, bottom row).

5. Results

5.1 Evaluation of the iterative PVC algorithm

Figure 21 shows a central slice of the uncorrected, noise-free, image volume after reconstruction (a), the PVE corrected image without (b) and with (c) the voxel filling fraction taken into account, and the true source distribution (d). There is virtually no visual difference between the images in figure 21c and 21d, implying a nearly perfect correction. It is also clear that the image quality is improved when PVC is performed according to Eq. 30, incorporating the voxel filling fraction. In this case, however, it does not affect quantitative values since evaluation was performed only for voxels where $F_X = 1$ to avoid voxels shared by object and background.

The accuracy of the correction is also illustrated in Figure 22 where profiles over the central column in images 21a, 21c, and 21d have been plotted. The partial-volume corrected distribution follows the true source distribution nearly perfect, while the uncorrected image suffers from PVE as expected. The error in mean count level in each VOI is given in Table 4.

a. **b.** **c.** **d.**

Figure 21: Uncorrected image (a), PV corrected image (b), PV corrected image with voxel filling fraction taken into account (c) and the true source distribution (d).

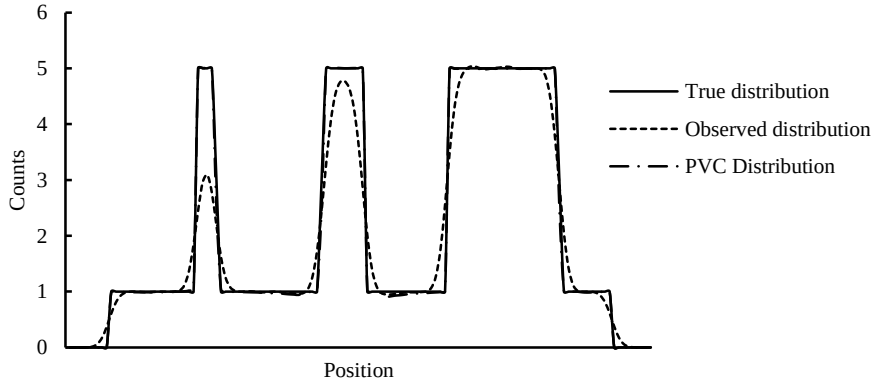

Figure 22: Profiles through the central column of Figure 21a, c and d. The PVC distribution shows excellent agreement with the true source distribution, and is not visible in this figure because of the overlap with the true distribution.

The mean number of counts in the 4 cm^3 sphere as a function of number of iterations of the PVC algorithm has been plotted in Figure 23. In this example, the initial value was chosen as the mean number of counts in the uncorrected image. Convergence is reached after just a few iterations (2-3), and the agreement with the true count level is excellent. Equivalent results were obtained for the other spheres. It is possible that additional iterations are necessary if the SPECT image is more complex in the sense of spill-over between several different structures. Since no apparent disadvantages in using a few additional iterations were found, 5 iterations were used in all following evaluations to avoid potential issues of incomplete convergence. The algorithm is fast, in the order of 1 second per iteration, and computing time is hence not an issue. Table 4 shows the error of mean count level for the background and each sphere before and after PVC. After correction, bias is reduced to -0.3 % or better for all regions with PBR, and -4.2 % or better with direct template reconstruction.

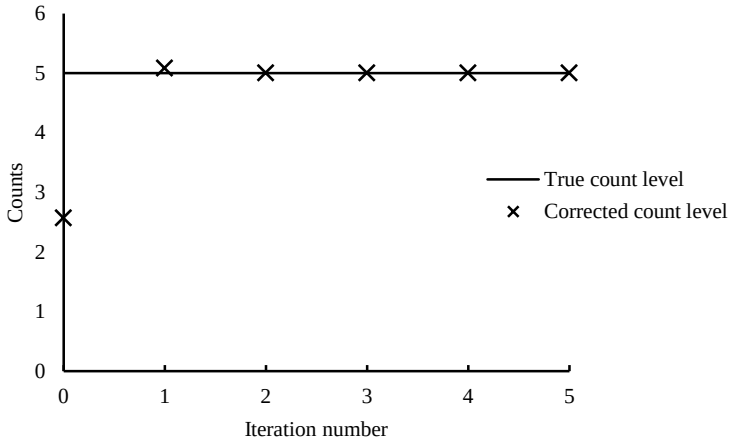

Figure 23: Mean count number in the 4 cm^3 sphere as a function of number of PVC iterations. A slight overcompensation can be seen after the first iteration, but convergence is reached after 2-3 iterations.

Table 4: Mean count level error ε (%) in each VOI before and after 5 iterations of PVC using direct reconstruction (PVC-DR) and perturbation based reconstruction (PVC-PBR) for the templates.

Object	No corr.	PVC-PBR	PVC-DR
Background	-5,2	-0,1	0,0
4 cm^3 sphere	-48,6	0,0	2,8
34 cm^3 sphere	-30,7	-0,3	-4,2
530 cm^3 sphere	-9,9	0,0	0,1

5.1.1 Noise sensitivity

The error in mean count level after PVC with PBR and DR for the different noise realizations is given in Table 5 and Table 6, respectively. It can be noted that the presence of noise degrades the quantitative accuracy (compare Table 4), which is especially prominent for the 34 cm^3 sphere. Both reconstruction methods produce approximately equivalent results for 50 and 10 million total counts. The PBR method is more sensitive to noise, and for 1 million counts the PVC fails completely and reduces the accuracy compared to the original image. In this case the corrected image has no visual resemblance to the original image. The DR method did however succeed in maintaining visual quality and reasonable quantitative accuracy even at 1 million counts. The subtraction as given by Eq. 28 leads to negative values in the PV corrected image, when the SPECT image is subject to noise. This is more prominent for PBR than DR, and extreme values become more frequent with increasing noise level.

Table 5: Mean count level error ε (%) in each VOI before and after PVC using the PBR method for template reconstruction, after Poisson noise corresponding to 1, 5, 10 and 50 million counts was added to the projected source distribution.

Total counts ($\cdot 10^6$)	Object							
	Background		4 cm^3 sphere		34 cm^3 sphere		530 cm^3 sphere	
	No corr.	PVC	No corr.	PVC	No corr.	PVC	No corr.	PVC
50	-5.3	-0.2	-48.0	0.6	-35.0	-10.4	-10.2	-0.7
10	-4.7	0.5	-46.5	1.6	-38.2	-21.5	-10.8	-2.3
5	-4.1	1.5	-49.6	-4.2	-37.7	-23.4	-11.3	-3.5
1	-1.8	62.7	-50.3	-29.5	-40.0	-60.9	-12.6	-14.3

Table 6: Mean count level error ε (%) in each VOI before and after PVC with direct reconstruction of templates, after Poisson noise corresponding to 1, 5, 10 and 50 million counts was added to the projected source distribution. Note that the uncorrected data is the same as in Table 5; it is included to simplify comparison.

Total counts ($\cdot 10^6$)	Object							
	Background		4 cm^3 sphere		34 cm^3 sphere		530 cm^3 sphere	
	No corr.	PVC	No corr.	PVC	No corr.	PVC	No corr.	PVC
50	-5.3	-0.1	-48.0	4.2	-35.0	-11.4	-10.2	-0.3
10	-4.7	0.5	-46.5	7.9	-38.2	-17.9	-10.8	-1.1
5	-4.1	1.0	-49.6	0.5	-37.7	-15.6	-11.3	-1.7
1	-1.8	3.4	-50.3	-3.0	-40.0	-20.7	-12.6	-3.6

It can be noted that the corrected values obtained for the 34 cm^3 is underestimated in all cases, and not as accurate as the results for the other objects. The underestimation increases with increasing noise level, but can also be noticed in the noise-free case. The reason for this is unknown but is probably related to the position of the sphere in the center of the phantom where the distance to the camera head is relatively large for all projection angles. For instance, a small mismatch between the modeling of attenuation in projection and reconstruction would be most prominent in this region. It can be noted that the 34 cm^3 sphere is not visible in the projection images at 1 million total counts because of attenuation and low SNR. The experiment will be repeated in future studies with interchanged locations of the spheres inside the phantom to investigate the reason for the discrepant result for the 34 cm^3 sphere.

5.2 XCAT phantom study

The error ε (%) in mean activity concentration for the kidneys, spleen and liver, before and after PVC is given in Table 7. The developed PVC method improves the error in mean activity concentration for all defined structures and different phantoms. For the kidneys, the error is improved from approximately -20 % to -1% when all templates were based on the true organ configuration in the phantom. The results obtained with kidney templates that were outlined with the automatic method are nearly equivalent. The maximum error in mean activity concentration in the kidneys for all phantoms is 2.5 % after correction, compared to -23 % in the uncorrected images. The measured values after PV correction are in good agreement with the true values, irrespective of method for kidney template definition.

Table 7: Error ε (%) in mean activity concentration for the four different phantoms before and after PVC, with two different methods of defining kidney templates. A negative sign indicates an underestimation.

		XCAT templates		Automatic segmentation	
Phantom	Structure	Uncorrected	PVC	Uncorrected	PVC
t1 (0.5 h p.i.)					
	Kidneys	-18.8	-0.6	-21.5	1,2
	Spleen	-23.1	-2.4	-28.7	-4.1
	Liver	-6.3	-0.5	-8.6	-1,3
t2 (24 h p.i.)					
	Kidneys	-19.6	-0.6	-22,4	1,8
	Spleen	-24.3	-0.9	-30,5	-3,0
	Liver	-8.2	-0.5	-11,2	-1,8
t3 (96 h p.i.)					
	Kidneys	-20.0	-1.1	-23.0	1.2
	Spleen	-24.7	-1.1	-30.9	-3.1
	Liver	-8.4	0.1	-11.6	-1.2
t4 (168 h p.i.)					
	Kidneys	-19.5	-0.8	-22.0	2.5
	Spleen	-24.5	-0.9	-30.8	-3.2
	Liver	-8.7	0.1	-12.0	-1.1

The spleen and liver templates are created from the XCAT phantom in both cases. In the case where all templates were generated from the phantom, the templates were re-sampled to the SPECT resolution by bilinear interpolation. Evaluation of mean activity concentration was then made for all voxels totally within the structure, *i.e.* for all voxels in the re-sampled template with value 1. In the case were the kidneys were automatically outlined in the SPECT image, the remaining templates were re-sampled by nearest neighbor interpolation to match the kidney templates. This is needed to assure that the sum of all templates equals one for all voxels to be corrected. The evaluation of activity concentration was also in this case performed for all voxels with value 1. Due to the different interpolation methods, the uncorrected values for the spleen and liver are not identical in these two cases as the VOIs are slightly different. By using nearest neighbor interpolation and evaluate count levels where T_X = 1, partial-volume effects due to discretization is avoided. This is the reason that the uncorrected mean activity concentrations are slightly higher when all templates were taken from the true organ setup in the phantom.

Reconstructed coronal SPECT slices with and without PVC correction is shown in Figure 24. It is evident that the visual appearance of the corrected image is strongly dependent on the defined templates. When the true XCAT VOIs were used as templates, the voxel filling fraction was incorporated in the correction, which reduces the jagged appearance in the corrected image.

The total correction factor *k* for the defined structures is given in Table 8. It can be noted that there are no major difference between the different time points, mainly because the source distribution is rather similar. Note the difference of the correction factor between the different organs.

Table 8: Total correction factor *k* for the different organs and different methods for defining the kidney VOI.

Phantom	Structure	XCAT templates	Automatic segmentation
t1 (0.5 h p.i.)			
	Kidneys	1.22	1.29
	Spleen	1.27	1.34
	Liver	1.06	1.08
t2 (24 h p.i.)			
	Kidneys	1.24	1.31
	Spleen	1.31	1.39
	Liver	1.08	1.11
t3 (96 h p.i.)			
	Kidneys	1.24	1.31
	Spleen	1.31	1.40
	Liver	1.09	1.12
t4 (168 h p.i.)			
	Kidneys	1.23	1.31
	Spleen	1.31	1.40
	Liver	1.10	1.12

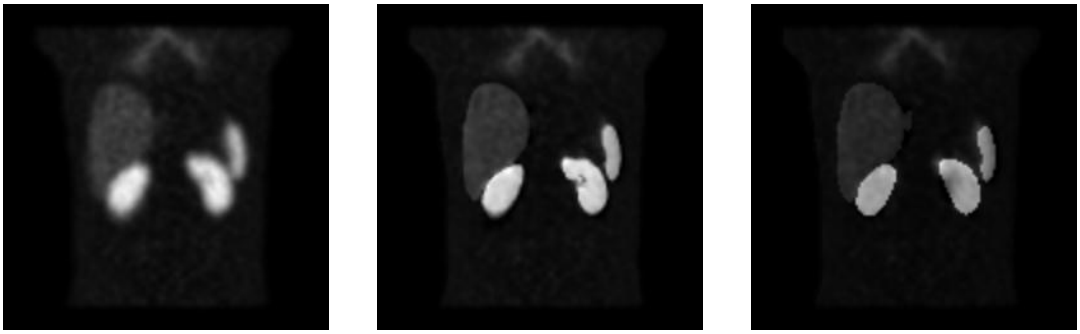

Figure 24: Coronal slice of reconstructed SPECT image for phantom t1 without correction (left), with PVC correction using true templates (middle) and with PVC correction using kidney templates defined by automatic segmentation of the SPECT image (right). Note that the voxel-filling fraction F has been used for the PVC in the middle image, since the templates were available in higher resolution, i.e. *smaller voxels.*

5.3 Clinical images

The obtained quantitative results for the kidneys, liver and spleen for patient 1 and patient 2 is demonstrated in Figure 25 and Figure 26, respectively. For the first patient, the uncorrected mean value for both kidneys and therapy sessions is 9.8 counts per voxel (CPV) using method 1 for template generation. The corresponding value after PVC is 14.5 CPV, giving k = 1.48. Using method 2, automatic segmentation of kidneys, k is equal to 1.41 with mean values 10.3 CPV prior to correction and 14.4 CPV after correction. Corresponding values for method 3 is 1.75, 10.9 CPV and 19.0 CPV, respectively. Before correction, all three methods produced approximately equivalent results but the mean count level is slightly higher with method 3 due to the more confined VOI. The partial-volume corrected count level is almost identical for method 1 and 2, but significantly higher for method 3. The values for the spleen and liver are essentially identical in all three cases since almost identical templates were used for these organs. They were only altered if there was an overlap with the kidneys, in which case the overlapping voxels were set to zero in the liver and spleen template.

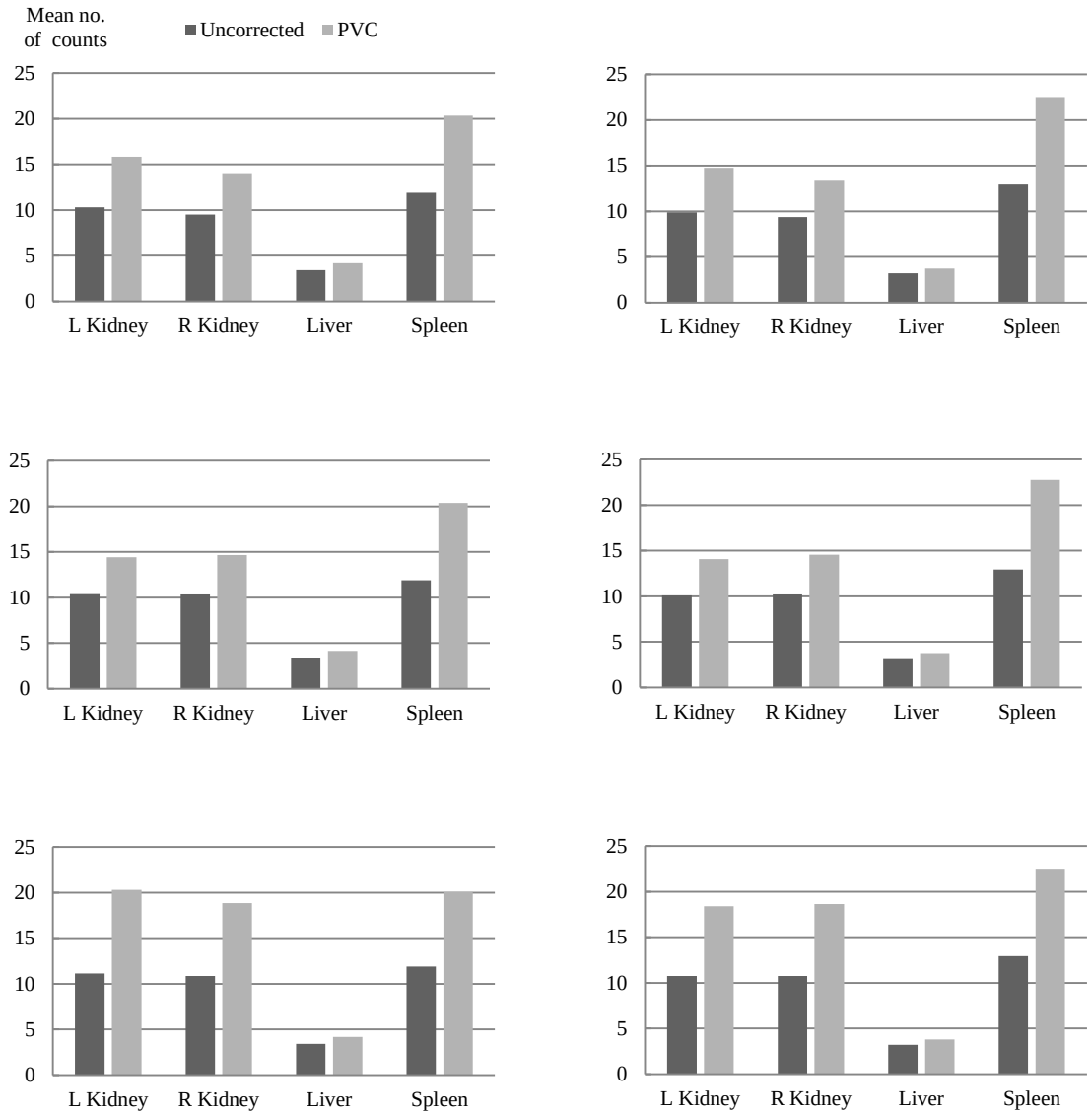

Figure 25: Mean number of counts in the defined organs for patient 1, therapy session 1 (left column) and session 2 (right column). Templates have been generated by manual outlining in a CT image (Method 1, top row), automatic segmentation on SPECT image (Method 2, middle row) and by previously outlined kidney VOI used for activity quantification (Method 3, bottom row).

For the second patient, the uncorrected mean values for both kidneys and therapy sessions are 11.1, 12.4 and 12.7 CPV for method 1, 2 and 3. After correction, corresponding values are 15.8, 17.0 and 21.5, yielding correction factors of 1.42, 1.38 and 1.69.

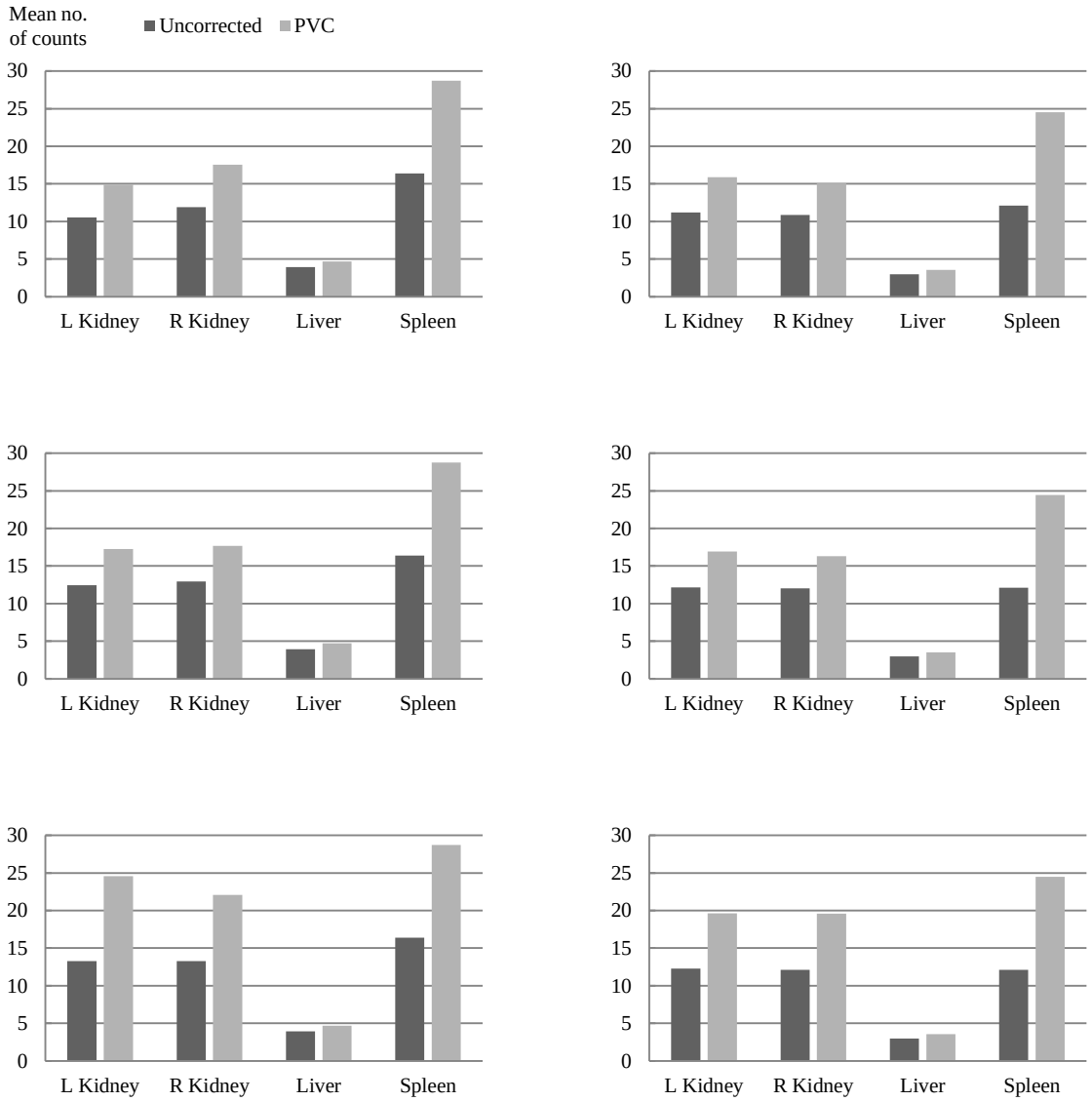

Figure 26: Mean number of counts in the defined organs for patient 2, therapy session 1 (left column) and session 2 (right column). Templates have been generated by manual outlining in a CT image (Method 1, top row), automatic segmentation on SPECT image (Method 2, middle row) and by previously outlined kidney VOI used for activity quantification (Method 3, bottom row).

A coronal slice of the reconstructed SPECT image with and without PVC for patient 1, therapy session 1 is shown in Figure 27, with the three different methods for defining the kidney VOIs. It is clear that Method 2 is preferable for defining the kidney VOI in terms of visual quality in the PV corrected image. The overall poor quality of the PV corrected images can be attributed to the difficulties in delineating structures on CT images due to the presence of artifacts and poor axial resolution.

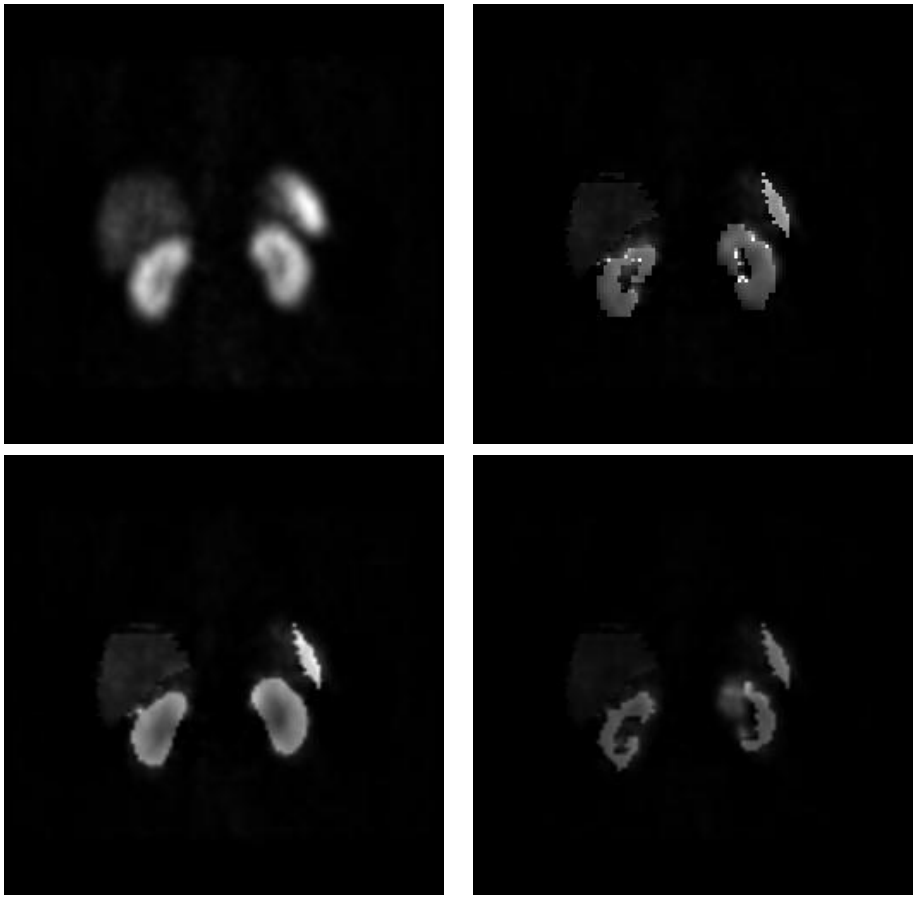

Figure 27: Coronal slice of reconstructed SPECT image for patient 1, therapy session 1. The images shown are uncorrected image (top left), and PV corrected images with kidney templates generated by Method 1 (top right), Method 2 (bottom left) and Method 3 (bottom right), respectively. Note that the appearance of the PVC corrected images is determined by the defined templates. The PVC images have been thresholded to suppress extreme pixel values.

In the clinical standard protocol, the SPECT images are reconstructed with 8 iterations OS-EM, using 6 angles per subset and compensation for attenuation, scatter and CDRF, but without explicit PVC. The VOI used for evaluation is the same as in method 3. Mean count levels obtained for the kidneys with the clinical protocol and with the current method using PVC, are shown in Figure 28. For several reasons discussed later, method 2 was considered as the "golden standard" to create the kidney templates, and therefore used in this comparison.

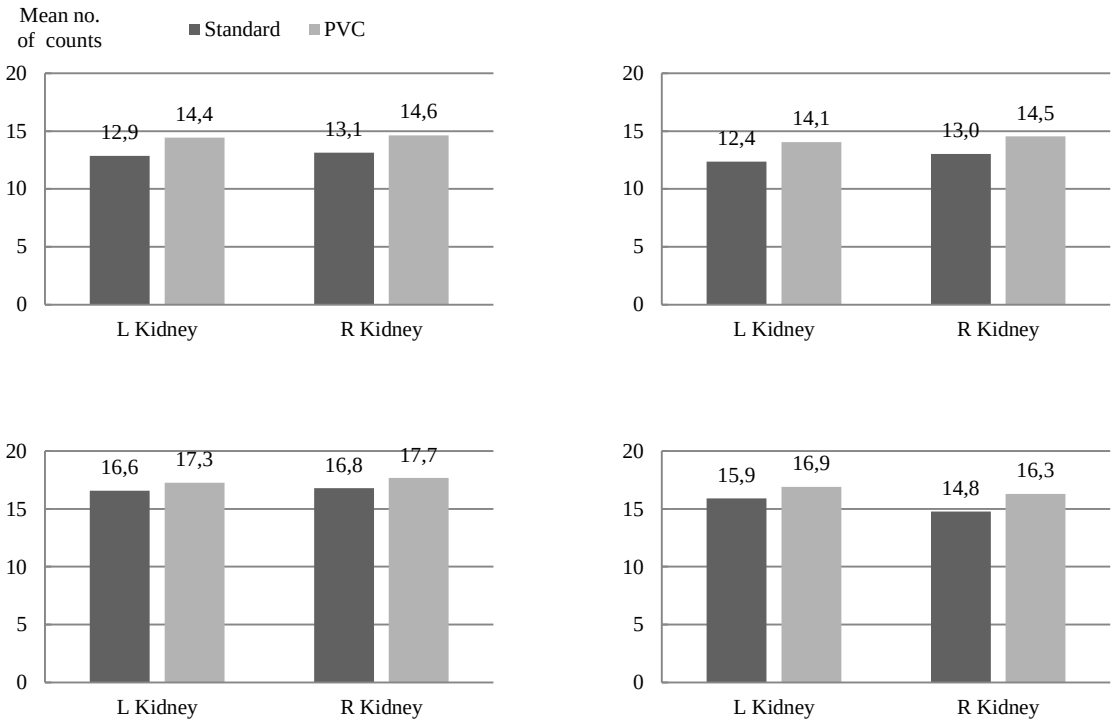

Figure 28: Mean number of counts in the left and right kidney for patient 1 (top row) and patient 2 (bottom row), therapy session 1 (left column) and session 2 (right column), obtained with the standard clinical method ("Standard"), and obtained with the current method with partial-volume correction ("PVC").

The current method with PVC results in approximately 10 % higher count levels than the standard method in all cases (range 5-14 %). No significant differences between the right and left kidney can be observed. The ratio of the results obtained with the current method to the results obtained with the standard method is given in Table 9.

Table 9: Ratio of mean count number obtained with the current method, including PVC, to mean count number obtained with the standard clinical method.

		Left kidney	Right kidney
Patient 1			
	Therapy 1	1.12	1.12
	Therapy 2	1.14	1.12
Patient 2			
	Therapy 1	1.04	1.05
	Therapy 2	1.06	1.10

6. Discussion

Visual quality of partial-volume corrected SPECT images
The template-based PVC method presented in this work is likely not a feasible approach for improving the visual quality of SPECT images, which has been suggested by other authors [7, 8]. The corrected image will have the appearance of the defined templates which are highly method- and/or user-dependent. With templates that are perfectly matched and aligned to the original source distribution, the corrected image will have a visual resemblance to the original distribution, but this is not possible in a realistic scenario when templates are defined with manual (or automatic) segmentation. This becomes obvious when comparing Figures 24 and 27. It is however possible that the PV corrected images can be improved with better tools for template definition, for instance if the VOI could be outlined in 3D instead of on transversal slices. The CT images from the clinical SPECT/CT system suffers from low contrast and streak artifacts, making manual outlining problematic. The current method of outlining VOIs on transversal slices (Method 1 and 3) results in discontinuities in coronal and sagittal slices in the corrected images, which is anatomically unrealistic and the quality of the PV corrected images is generally poor. Other approaches for defining VOI:s for this application is therefore preferable, for instance the automatic segmentation method (Method 2). It is also noticeable in Figure 27 that there are extreme values in the PVC images, especially for Method 1 and 3. In this study, 20 iterations was used in the reconstruction compared to 10 iterations in the phantom study. As mentioned previously, extreme values become more frequent with increasing noise level and it is therefore appropriate to use as few iterations as possible without neglecting convergence in the structures of interest.

Incorporating the voxel filling fraction into the correction algorithm improves the quality of PVC images by normalizing the correction factor with the fractional presence of the tissue in the voxel to be corrected. This is illustrated in figure 21 and 24. This correction only affects edge voxels that are shared between different structures, and is not important for quantification purposes as long as the edge voxels only constitute a small fraction of the defined VOI. The voxel filling fraction can only be utilized if the templates are available with smaller voxel size, and is thus not applicable when the segmentation is performed on the SPECT image. As discussed above, accurate methods are required for VOI definition in order to be able to improve the visual quality in the PV corrected images. Given the current possibilities of VOI definition and poor quality of the CT images, this is not a realistic aim. For this reason, the voxel filling fraction is of secondary importance.

Quantitative results
The evaluation of the PVC algorithm showed that a virtually perfect correction was achieved under perfect conditions, using the iterative approach and perturbation based reconstruction, previously described. The presence of noise reduced the accuracy of the method, and the impact was larger when the perturbation based method was used for template reconstruction. The iterative approach for estimation of mean count number was shown to be successful and considerably increased the robustness of the PVC correction method. It has two major advantages. Firstly, the final result becomes insensitive to the initial estimate of mean count level. This is most likely due to the fact that the PVC correction in most cases is rather small, and since the estimate of the mean count level at the second iteration is calculated over the entire VOI, this value will be fairly good regardless of the initial estimate. Secondly, the result becomes insensitive to the volume over which the mean count level is evaluated for the different structures. Without the iterative method presented here, the choice of volume would have to be optimized, to make the estimate of the mean count level unaffected by partial-volume effects, which in practice is impossible for small structures. Possibly, one could apply spill-out correction for small structures before evaluation the mean count level, but this would result in an overestimation since spilled-in counts have not been subtracted. Subtracting spilled-in counts would also be difficult, since the estimated spill-in will be based on the mean value in other regions, also affected by PVE. These issues are avoided with the iterative method. In addition, the order in which the different structures are corrected seems to have a negligible effect.

In the XCAT phantom study, the PVC method was tested under realistic conditions with clinically relevant source distributions. In this case, the imaging system (SIMIND) and the analytical projector were not identical, and scattered photons were included in the SIMIND simulated projections. In addition, different routines are used in the analytical projector and SIMIND for determination of projection distances, and they do produce similar but not identical results. The projection distances determined in SIMIND were available, and could have been used in the analytical projector, but this approach would have excluded a potential source of error present when working with clinical images. By outlining of the kidneys with the automatic method, the PVC method was also tested with more realistic templates. For the kidneys, the error in activity estimate ranged from -18.8 % to -23.0 % in the uncorrected images, which was improved to the range -1.1 to 2.5 with PVC. In general, excellent agreement between measured PVC values and true values was achieved for all defined organs, despite differences in size and shape, since the method inherently takes these factors into account. For instance, the correction factor for the liver is smaller than for the kidneys and spleen, mainly due to the larger volume. Similar results were obtained using both segmentation methods to create the kidney templates, which indicates that accurate quantitative results can be obtained also with realistic templates. It should however be emphasized that only one noise realization was used for this evaluation, which is a limitation of the study. An accuracy and precision estimation will however be carried out in future studies by utilizing multiple noise realizations at a representative count level. The efficiency of CDRF compensation in reconstruction in terms of count recovery will also be considered.

The developed PVC method was also tested on clinical images with different methods for outlining the kidney VOIs used to generate templates. The methods did not produce equivalent results, which indicate that the quantitative accuracy of the method is sensitive to the organ delineation. This is further discussed in the next section. The comparison between the current method and the standard clinical method is also discussed below.

Dependence on VOI definition

Throughout this work, several different methods were used for outlining of structures. Since the outlined VOI is used both for activity quantification and to create the template, the method was expected to be sensitive to organ delineation. In the XCAT phantom study, templates were acquired either directly from the organ configuration in the phantom or generated by automatic segmentation of the reconstructed SPECT image. It should be noted that a small spatial or COR mismatch (less than 1 pixel) between projections from SIMIND and the analytical projector was discovered, leading to a small spatial mismatch also between the SPECT image and the reconstructed templates. The origin of this mismatch has yet not be found, but can be considered to be a source of error also present in clinical images. By outlining of the kidneys with the automatic method, the PVC method was also tested with realistic templates. In both cases, the bias in activity estimate for the kidneys was reduced to 2.5 % or better, implying that the method produces reliable results also with realistic templates and small spatial mismatches. The sensitivity to organ delineation was further addressed when PVC was performed on the clinical images, with three different approaches for outlining of the kidney VOI. By studying Figure 25 and 26, it is clear that method 3 (used in the standard clinical protocol) produces results that are inconsistent with the results obtained with the two other methods. The reason for this is that the size and shape of the defined template do not correspond to the anatomical kidney (Figure 20). Since the defined VOI is considerably smaller than the kidney and have a more irregular shape the spill-out will be largely overestimated, and the following PVC will therefore overcompensate. Method 3 was included to investigate if it was possible to perform PVC with already existing kidney VOIs which would have made it possible to process a large image material without defining new VOIs for all patients. It is however evident that these VOIs are unsuitable for this PVC method. Method 1 and 2 for generating kidney templates gives nearly equivalent results, with correction factors that are more in line with what was seen in the phantom study. This also indicates that the method is not very sensitive to the delineation as long as the size and shape of the VOI resembles the anatomical size and shape with reasonable

accuracy. This statement needs however to be verified in a systematic study, for instance by eroding and dilating the VOI and studying the effects on activity estimates after PVC. When using method 1, a difference in count level between the left and right kidney can be seen, which is most likely caused by the operators lack of experience with regards to organ delineation. This difference is not seen when automatic segmentation is used (method 2) or when an experienced operator is responsible for defining the VOI (method 3).

Method 2 for VOI definition has several advantages. Firstly, the influence of the operator is diminished. Secondly, the templates are smooth in all three planes and show good visual resemblance with the anatomical shape of the kidneys. In addition, segmentation is performed on the SPECT image which guarantees perfect spatial alignment between the template and SPECT image. This is not guaranteed even when using hybrid SPECT/CT systems. The effects of a spatial misregistration between SPECT and CT images were not explicitly studied. It is however believed that there are larger quantitative uncertainties introduced when manually outlining the VOI on the SPECT image than what would be caused by a minor misregistration between SPECT and CT, based on the low quality and thick slices (10 mm) of the CT images obtained with the Hawkeye unit. Large spatial mismatches can easily be detected by visual assessment, for instance on a fused SPECT/CT image. If there are inconsistencies between anatomical and functional images, it is likely better to use the functional image when defining the template since the underlying assumption of the PVC method is that the templates represents regions with uniform activity uptake. It is obviously required that the region boundaries are sufficiently distinct to allow segmentation. Using the SPECT image for segmentation is also preferable since has an isotropic voxel size of 4 mm, whereas the slice thickness of the CT image is 10 mm, resulting in a "jagged" kidney template when the CT image is used for outlining of the organ. This is clearly noticeable in the coronal and sagittal views in Figure 20. By using the automatic segmentation method which operates in 3D, these issues are avoided.

Using method 1 and 2, the mean count level after PVC is roughly 40 % higher than the count level obtained without correction for all four images. In the phantom study, the correction factor was smaller, approximately 1.3. The main reason for the difference is likely the difference in kidney volume, which is larger in the phantom. In addition, the couch of the SPECT/CT system results in larger projection distances in the clinical situation than in the simulations. This affects the spatial resolution negatively and increases PVE. The larger PV correction for the clinical images can also be due to the fact that the spill-in contribution from the spleen and liver is underestimated in the clinical images. The outlining of these organs was performed with purpose of activity quantification by intentionally excluding the outer rims that are known to be affected by PVE, rather than following the anatomical outline, in the same manner as for the kidneys with method 3. The size of the liver and spleen is therefore underestimated and the spatial separation between the templates will be larger than the actual distance between the organs, resulting in a too small correction for spill-in to the kidneys. This issue will be addressed in further studies where the spill-over contribution between the defined structures will be calculated explicitly. The mean count level after PVC in the spleen and liver is also likely to be too high in all cases because of the manner in which the outlining has been performed. This is also reflected in the high correction factor for the liver and spleen in the clinical images compared to the corresponding values for the simulated images.

Sensitivity to non-uniform activity distribution

The developed method for partial-volume correction is based on the assumption that each defined template represents a volume with uniform activity concentration. The uptake of ^{177}Lu-Octrotate in the kidneys is however concentrated to the cortex, with lower uptake in the medulla [3]. The impact of assuming a uniform activity concentration in the kidneys when performing PVC has yet not been fully studied. This is planned to be done by Monte Carlo simulation with the XCAT phantom, with different but realistic cortex/medulla activity ratios. If the assumption of uniform uptake results in a significance bias, an additional correction may be required. Ideally, the PVC should be performed with separate templates for the kidney cortex and the medulla. This is however, currently, not a realistic approach since it is impossible to

differentiate between the kidney cortex and medulla in the images obtained from the Hawkeye CT unit. The general background region, as defined by the rest-of-body template, also contains a non-uniform activity distribution. The impact of assuming a homogenous concentration within this region has not been evaluated. This will be performed by similar Monte Carlo simulations with a more complex activity distribution, for instance by defining explicit concentrations for intestines, lungs, arteries and veins. The effect of assuming uniform uptake in the background region is however believed to be relatively small since it is the total spill-in contribution to the organs that is of interest.

Omitting scattered photons as a source of blurring

Photon scatter contributes to the blurring of SPECT images and are thus of importance with regards to the partial-volume effect. Explicit scatter modeling has been omitted in this work, mainly due to the complexity in modeling the spatially variant and object dependent scatter response function. Ideally, scattered photons should be included in the projected templates since the intention is to model the image acquisition as closely as possible. Since the scatter contribution was omitted when forward projecting the templates, scatter correction was not employed during reconstruction. This essentially means that the reconstructed templates are free of any effects caused by scattered photons and scatter correction in reconstruction. The SPECT image, on the other hand, is affected by both. However, under the assumption that the scatter correction is perfect, there will be no effect of scattered photons on the spatial resolution, and the template will thus represent a true map of how counts are being blurred during the image formation process. In the phantom study, the simulated projections included scattered photons within the 20 % energy window centered around 208 keV. SPECT reconstruction was performed with scatter correction, whereas the projected templates were reconstructed without such correction. The accurate agreement between true activity concentration and measured PV corrected activity concentration for all phantoms and organs indicate that the scatter correction method sufficiently reduces the loss of spatial resolution caused by scattered photons. The consequences of omitting scatter in the projected templates in context of perturbation based reconstruction are further discussed in the next section.

Perturbation-based reconstruction

The principal idea of the perturbation based reconstruction is to reconstruct the templates in exactly the same way as the SPECT image and letting the spatial resolution in the reconstructed templates be determined by the SPECT image. In this work, the SPECT image to be corrected for PV is reconstructed with correction for scatter and attenuation, whereas the templates are reconstructed with correction for attenuation only. This means that a SPECT image $\boldsymbol{M}$ is first reconstructed without scatter correction only to calculate the templates $\boldsymbol{T}$ according to Eq. 27, and then discarded. Another SPECT image is then reconstructed, with scatter correction, and the PVC is subsequently performed on this image set. If scatter correction would have been included in template reconstruction, the reconstructed templates would be incorrect since the analytical projector does not model scattered photons. Since the templates and SPECT image are reconstructed with different corrections, the rationale for using the perturbation method falls. It was however included for several reasons. Further development of this PVC method should include scattered photons in the projected templates. This can be achieved for instance by using SIMIND to project the templates instead of using the analytical projector. Another possible approach is to model the scatter contribution analytically, for instance be means of ESSE [44] or the APDI (analytical photon distribution with interpolation) [49] method. As previously mentioned, analytical projection of the templates is much less time consuming and more feasible in terms of practical usability, compared to Monte Carlo simulations. It is possible that the forward projector used in the OS-EM reconstruction program developed by Frey's group [10] could be extracted and used to project the templates, thereby including the scatter contribution with the ESSE method. Regardless of scatter estimation method, the templates and SPECT image can be reconstructed with exactly the same method and parameters if scattered photons are included in the forward projection of templates. In this case, the perturbation based method will be principally correct to use. Despite this principal shortcoming, it is believed that

the PBR results in a blurring of the reconstructed templates that is more similar to the SPECT image than if the templates were reconstructed directly, even though the SPECT image is scatter corrected and the templates are not. Previous investigations have also shown that the perturbation method is of greater importance when reconstruction is performed with CDRF compensation [11]. This is most likely due to the very slow convergence rate of iterative methods when CDRF compensation is used in the reconstruction. In this work, CDRF compensation was not employed as it increases the reconstruction time significantly and was shown to not improve quantitative accuracy after PVC with the present method. CDRF compensation is however important for improving image quality and is currently used in the standard clinical protocol. If this PVC method is to be used in clinical practice, PBR is believed to be of greater importance.

A comparison between PBR and direct reconstruction of the templates was performed with the simple geometrical phantom. The measured emission set is subjected to noise and non-uniform count distribution, which will propagate to the reconstructed templates when using PBR. Performing PVC with noisy reconstructed templates will result in an increased noise level in the corrected image. The noise sensitivity test (section 4.1.1 and 5.1.1) revealed that the PVC method is more sensitive to noise if PBR is used for template reconstruction. As shown in Table 4, PVC with templates reconstructed using PBR gives more accurate quantitative result compared to PVC with templates which have been directly reconstructed when noise is absent. With increasing noise level, it becomes more favorable to perform PVC with noise-free reconstructed templates which are obtained by direct reconstruction. This is evident from Table 5 and Table 6. Since the noise level of the SPECT images is affected by many factors, such as the number of iterations in the reconstruction and use of low-pass post-filtering, there is no exact count level over which PBR is generally superior to direct reconstruction. In this example, 20 iterations with 6 subsets of OS-EM were used for reconstruction, as a compromise between convergence and noise amplification. A noise suppressing post-reconstruction Gaussian filter was also employed. It is likely that the noise sensitivity could be reduced by using fewer iterations, or by increasing the low-pass filtering. Generally, the number of iterations must be sufficiently large to allow convergence of counts in the structure of interest. It is however possible that PVC using PBR also could compensate for the loss of counts due to incomplete convergence, as the reconstructed templates are maps of how counts are being spread also by the reconstruction process. The dependence of quantitative accuracy after PVC on the number of iterations used in reconstruction has not been studied in this work, but could be subject to future research. The effects of image reconstruction on the final resolution in SPECT images are secondary to the effects of resolution in the projection images, mainly determined by the PSF. Given the overall uncertainty of quantitative SPECT and finally absorbed dose calculations, the benefit of direct reconstruction in terms of reduced noise sensitivity could outweigh the somewhat reduced quantitative accuracy. The possible influence of CDRF compensation in reconstruction should however be considered.

Practical considerations

The developed PVC method requires outlining of a number of structures and generation of templates. It is assumed that each defined structure represents a distinctive volume of uniform activity concentration. In practice, this is impossible to achieve because of the generally complex activity distribution in realistic images and the labor required for the outlining of structures. In this work, templates were only defined for the kidneys, the liver and the spleen, whereas the remainder was included in a rest-of-body template. This is evidently an approximation, since the bio-distribution of ^{177}Lu-Octrotate is much more complex. The PVC method was however designed with intention to be practical, and defining more templates would be both difficult and time-consuming. It is also worth to mention that the computation time for reconstructing templates can be significant, especially if CDRF compensation is employed which also requires an increased number of iterations. The reason for defining specific templates for the liver and spleen is their relatively high and uniform activity uptake, and the proximity to the kidneys which could result in a significant spill-over contribution. It is possible that PVC for the kidneys can be performed with reasonable accuracy, using only

templates for the kidneys and grouping all other organs into a rest-of-body-template. The spill-over contribution between the structures was not studied explicitly, and whether it is necessary to define templates for organs other than the kidneys is subject to future research. Calculating spill-over contributions is a relatively straight-forward task and is intended to be done in the near future. Ideally, it would be desirable to outline some general guidelines on when it is necessary to define an individual template and when the organ can be included in a general background. This would be especially beneficial if the PVC method is adapted for other applications. The possible improvement in accuracy of the method should also be weighed against the effort and time required to outline additional organs. Automatic segmentation routines, as the method developed by Gustafsson [48] and used for outlining of the kidneys in this work is a promising tool in this context. The high activity uptake in the spleen allows for automatic segmentation also of this organ. In addition, the results from the XCAT phantom study indicated that anatomical images is not always required for template generation, since good quantitative results after PVC were obtained also when the kidney templates were generated by means of automatic segmentation.

Possible dosimetric consequences

The maximum range of the β-particles from ^{177}Lu in tissue is approximately 2 mm, which is smaller than the SPECT voxel size. For dosimetry calculations, all energy can thus be considered to be locally absorbed in each voxel, which simplifies dosimetry calculations significantly. The mean absorbed dose rate to the kidneys is hence proportional to the mean activity concentration and mean count level, neglecting cross-dose from γ-radiation which can be approximated as a small additive contribution [50]. The mean absorbed dose is calculated by integration over time, enabled by the set of images acquired at different times post injection. The comparison between the current method and the standard clinical method with regards to mean count level in the kidney VOI is presented in Figure 28 and Table 9. Method 2 (automatic segmentation) was used to generate the kidney template in this comparison for reasons mentioned above. The result suggests that the actual activity concentration in the kidneys is underestimated by approximately 10 % with the standard clinical protocol. This could have consequences for the treatment course of the patient, as the mean absorbed dose in this case also would be underestimated by roughly the same amount. These findings should however be considered very preliminary, and further assessments on a larger patient material is required before conclusions can be drawn. For instance, the total correction factor k is larger for the clinical images than for the patient images which may indicate on overcompensation. The reason for this needs to be further considered. As previously mentioned, the efficacy of CDRF compensation for activity quantification purposes will be investigated, and it is possible that explicit PVC is not needed for this particular application. The result from the patient study indicates that complete count recovery with CDRF compensation is not obtained, but it is possible that this is a result of incomplete convergence. In this case, the accuracy could easily be improved by increasing the number of iterations used in OSEM reconstruction.

7. Future prospects

The developed PVC method has yet not been evaluated by physical measurements. To validate the method, PVC should be performed as a part of quantitative ^{177}Lu SPECT imaging with a physical phantom. Recently, a kidney and liver phantom (LK-S Kyoto Liver/Kidney phantom) was purchased and quantitative measurements and evaluation of the method are planned to be carried out in the near future. Measurements of the PSF for the camera system with ^{177}Lu should also be performed to verify the Monte Carlo simulations. Other experimental setups are also possible for validation. As previously mentioned, additional work will be carried out to investigate spill-over contributions between different structures and the influence of non-uniform activity concentrations within the defined regions. Also, it is desirable to include scattered photons in the analytical projector since scatter correction then would be employed in template reconstruction. In this case, the templates and the SPECT image can be reconstructed using identical parameters and corrections, which is the theoretical basis for perturbation based reconstruction. Hopefully, further development and application of this method can be used in a future publication. Comparison will also be made with results obtained using CDRF compensation in SPECT reconstruction for reducing PVE.

Acknowledgments

I would like to express my gratitude to my supervisors, Michael Ljungberg and Katarina Sjögreen Gleisner for their patience in guiding and helping me through this project. I would also like to thank Karin Wingårdh for practical assistance using the SPECT camera and working with the clinical images. Finally, I would like to express my gratitude to Johan Gustafsson for valuable discussions and collaboration during this and previous semesters.

References

1. *Isotopterapier på svenska sjukhus 1994 - 2010*. 2011 [cited 2011 06 13]; Available from: www.isotopterapi.se.
2. Garkavij, M., et al., *^{177}Lu-[DOTA0,Tyr3] octreotate therapy in patients with disseminated neuroendocrine tumors: Analysis of dosimetry with impact on future therapeutic strategy.* Cancer, 2010. **116**(S4): p. 1084-1092.
3. Konijnenberg, M., et al., *Radiation Dose Distribution in Human Kidneys by Octreotides in Peptide Receptor Radionuclide Therapy.* Journal of Nuclear Medicine, 2007. **48**(1): p. 134-142.
4. Cremonesi, M., et al., *Recent issues on dosimetry and radiobiology for peptide receptor radionuclide therapy.* Q J Nucl Med Mol Imaging, 2011. **55**(2): p. 155-67.
5. Rousset, O.G. and H. Zaidi, *Correction for Partial Volume Effects in Emission Tomography*, in *Quantitative Analysis in Nuclear Medicine Imaging*, H. Zaidi, Editor. 2006, Springer US. p. 236-271.
6. Da Silva, A.J., et al., *Absolute quantification of regional myocardial uptake of 99mTc-sestamibi with SPECT: experimental validation in a porcine model.* J Nucl Med, 2001. **42**(5): p. 772-9.
7. Pretorius, P.H. and M.A. King, *Diminishing the impact of the partial volume effect in cardiac SPECT perfusion imaging.* Med Phys, 2009. **36**(1): p. 105-15.
8. Boening, G., P.H. Pretorius, and M.A. King, *Study of Relative Quantification of Tc-99 m With Partial Volume Effect and Spillover Correction for SPECT Oncology Imaging.* IEEE Trans Nucl Sci, 2006. **53**(3): p. 1205-1222.
9. Shcherbinin, S. and A. Celler, *An enhancement of quantitative accuracy of the SPECT/CT activity distribution reconstructions: Physical phantom experiments.* Comput Med Imaging Graph, 2010. **34**(5): p. 346-53.
10. He, B., et al., *A Monte Carlo and physical phantom evaluation of quantitative In-111 SPECT.* Physics in medicine and biology, 2005. **50**(17): p. 4169-4185.
11. Du, Y., B.M. Tsui, and E.C. Frey, *Partial volume effect compensation for quantitative brain SPECT imaging.* IEEE Trans Med Imaging, 2005. **24**(8): p. 969-76.
12. Segars, W.P., et al., *4D XCAT phantom for multimodality imaging research.* Med Phys, 2010. **37**(9): p. 4902-15.
13. Segars, W.P. and B. Tsui, *MCAT to XCAT: The Evolution of 4-D Computerized Phantoms for Imaging Research.* Proceedings of the IEEE, 2009. **97**(12): p. 1954-1968.
14. Anger, H.O., *Scintillation Camera.* Review of Scientific Instruments, 1958. **29**(1): p. 27-33.
15. Siegel, J.A., et al., *MIRD Pamphlet No. 16: Techniques for Quantitative Radiopharmaceutical Biodistribution Data Acquisition and Analysis for Use in Human Radiation Dose Estimates.* Journal of Nuclear Medicine, 1999. **40**(2): p. 37S-61S.
16. Fleming, J.S., *A technique for the absolute measurement of activity using a gamma camera and computer.* Physics in medicine and biology, 1979. **24**(1): p. 176-180.
17. King, M.A., et al., *Attenuation, Scatter, and Spatial Resolution Compensation in SPECT*, in *Emission Tomography (First Edition)*, M.N. Wernick and J.N. Aarsvold, Editors. 2004, Academic Press: San Diego. p. 473-498.
18. Tsui, B.M.W. and E.C. Frey, *Analytic Image Reconstruction Methods in Emission Computed Tomography*, in *Quantitative Analysis in Nuclear Medicine Imaging*, H. Zaidi, Editor. 2006, Springer US. p. 82-106.
19. Hutton, B.F., J. Nuyts, and H. Zaidi, *Iterative Reconstruction Methods*, in *Quantitative Analysis in Nuclear Medicine Imaging*, H. Zaidi, Editor. 2006, Springer US. p. 107-140.
20. Kuhl, D.E. and R.Q. Edwards, *Image Separation Radioisotope Scanning.* Radiology, 1963. **80**(4): p. 653-662.
21. Kinahan, P.E., M. Defrise, and R. Clackdoyle, *Analytic Image Reconstruction Methods*, in *Emission Tomography (First Edition)*, M.N. Wernick and J.N. Aarsvold, Editors. 2004, Academic Press: San Diego. p. 421-442.
22. Miller, M.I., D.L. Snyder, and T.R. Miller, *Maximum-Likelihood Reconstruction for Single-Photon Emission Computed-Tomography.* Nuclear Science, IEEE Transactions on, 1985. **32**(1): p. 769-778.
23. Shepp, L.A. and Y. Vardi, *Maximum Likelihood Reconstruction for Emission Tomography.* Medical Imaging, IEEE Transactions on, 1982. **1**(2): p. 113-122.
24. Lalush, D.S. and M.N. Wernick, *Iterative Image Reconstruction*, in *Emission Tomography (First Edition)*, M.N. Wernick and J.N. Aarsvold, Editors. 2004, Academic Press: San Diego. p. 443-472.
25. Hudson, H.M. and R.S. Larkin, *Accelerated image reconstruction using ordered subsets of projection data.* Medical Imaging, IEEE Transactions on, 1994. **13**(4): p. 601-609.

26. Liow, J.S. and S.C. Strother, *The convergence of object dependent resolution in maximum likelihood based tomographic image reconstruction.* Phys Med Biol, 1993. **38**(1): p. 55-70.
27. Pan, T.-S., et al., *Influence of OSEM, elliptical orbits and background activity on SPECT 3D resolution recovery.* Physics in medicine and biology, 1997. **42**(12): p. 2517-2529.
28. Frey, E.C. and B.M.W. Tsui, *Collimator-Detector Response Compensation in SPECT*, in *Quantitative Analysis in Nuclear Medicine Imaging*, H. Zaidi, Editor. 2006, Springer US. p. 141-166.
29. Sorenson, J.A. and M.E. Phelps, *Physics in nuclear medicine*. 2nd ed. 1987: Grune & Stratton.
30. Hoffman, E.J., S.-C. Huang, and M.E. Phelps, *Quantitation in Positron Emission Computed Tomography: 1. Effect of Object Size.* Journal of Computer Assisted Tomography, 1979. **3**(3): p. 299-308.
31. Rousset, O.G., Y. Ma, and A.C. Evans, *Correction for Partial Volume Effects in PET: Principle and Validation.* Journal of Nuclear Medicine, 1998. **39**(5): p. 904-911.
32. Pretorius, P.H., et al., *Reducing the influence of the partial volume effect on SPECT activity quantitation with 3D modelling of spatial resolution in iterative reconstruction.* Physics in medicine and biology, 1998. **43**(2): p. 407-420.
33. Kessler, R.M., J.R. Ellis, and M. Eden, *Analysis of emission tomographic scan data: limitations imposed by resolution and background.* Journal of Computer Assisted Tomography, 1984. **8**(3): p. 514-22.
34. Tsui, B.M.W., et al., *Implementation of simultaneous attenuation and detector response correction in SPECT.* Nuclear Science, IEEE Transactions on, 1988. **35**(1-part-1-2): p. 778-783.
35. Dewaraja Yuni, K., F. Koral Kenneth, and A. Fessler Jeffrey, *Regularized reconstruction in quantitative SPECT using CT side information from hybrid imaging.* Physics in medicine and biology, 2010. **55**(9): p. 2523-2539.
36. Shcherbinin, S. and A. Celler, *Assessment of the severity of partial volume effects and the performance of two template-based correction methods in a SPECT/CT phantom experiment.* Physics in medicine and biology, 2011. **56**(16): p. 5355-5371.
37. *IDL*, ITT Visual Information Solutions: Boulder, CO.
38. Zeng, G.L. and G.T. Gullberg, *Frequency domain implementation of the three-dimensional geometric point response correction in SPECT imaging.* Nuclear Science, IEEE Transactions on, 1992. **39**(5-part-1-2): p. 1444-1453.
39. McCarthy, A.W. and M.I. Miller, *Maximum likelihood SPECT in clinical computation times using mesh-connected parallel computers.* Medical Imaging, IEEE Transactions on, 1991. **10**(3): p. 426-436.
40. Wallis, J.W. and T.R. Miller, *An optimal rotator for iterative reconstruction.* Medical Imaging, IEEE Transactions on, 1997. **16**(1): p. 118-123.
41. Ljungberg, M. and S.E. Strand, *A Monte Carlo program for the simulation of scintillation camera characteristics.* Computer Methods and Programs in Biomedicine, 1989. **29**(4): p. 257-272.
42. Ljungberg, M., A. Larsson, and L. Johansson, *A new collimator Simulation in SIMIND based on the delta-scattering technique.* IEEE Transactions on Nuclear Science, 2005. **52**(5): p. 1370-1375.
43. Berger, M.J. and J.R. Hubbell, *XCOM: Photon Cross-sections on a Personal Computer*. 1987, National Bureau of Standards: Washington DC.
44. Frey, E.C. and B.M.W. Tsui, *A new method for modeling the spatially-variant, object-dependent scatter response function in SPECT.* Nuclear Science Symposium, 1996. Conference Record., 1996 IEEE, 1996. **2**: p. 1082-1086 vol.2.
45. Kwekkeboom, D.J., et al., *[177Lu-DOTAOTyr3]octreotate: comparison with [111In-DTPAo]octreotide in patients.* Eur J Nucl Med, 2001. **28**(9): p. 1319-25.
46. Esser, J.P., et al., *Comparison of [(177)Lu-DOTA(0),Tyr(3)]octreotate and [(177)Lu-DOTA(0),Tyr(3)]octreotide: which peptide is preferable for PRRT?* Eur J Nucl Med Mol Imaging, 2006. **33**(11): p. 1346-51.
47. Forrer, F., et al., *A comparison of (111)In-DOTATOC and (111)In-DOTATATE: biodistribution and dosimetry in the same patients with metastatic neuroendocrine tumours.* Eur J Nucl Med Mol Imaging, 2004. **31**(9): p. 1257-62.
48. Gustafsson, J., *Automatic segmentation of SPECT/CT images using a deformable surface model based on Fourier descriptors with application in radionuclide therapy*. 2011, Medical Radiation Physics, Lund University: Lund.
49. Vandervoort, E., et al., *Implementation of an Analytically Based Scatter Correction in SPECT Reconstructions.* IEEE Transactions on Nuclear Science, 2005. **52**(3-part-1): p. 645-653.
50. Ljungberg, M. and K. Sjögreen-Gleisner, *The accuracy of absorbed dose estimates in tumours determined by Quantitative SPECT: A Monte Carlo study.* Acta Oncologica, 2011. **50**(6): p. 981-989.